J. Fluid Mech. (1990), *vol.* 213, *pp.* 313–348
Printed in Great Britain

A numerical study of the turbulent Ekman layer

By G. N. COLEMAN[1], J. H. FERZIGER[1] AND P. R. SPALART[2]

[1] Department of Mechanical Engineering, Stanford University, Stanford CA 94305, USA

[2] NASA Ames Research Center, Moffett Field CA 94035, USA

(Received 11 October 1988 and in revised form 25 August 1989)

The three-dimensional time-dependent turbulent flow in a neutrally stratified Ekman layer over a smooth surface is computed numerically by directly solving the Navier–Stokes equations. All the relevant scales of motion are included in the simulation so that no turbulence model is needed. Results of the simulations indicate that the horizontal component of the rotation vector has a significant influence on the turbulence; thus the 'f-plane' approximation fails. Differences as large as 20% in the geostrophic drag coefficient, u_*/G, and 70% in the angle between the freestream velocity and the surface shear stress are found, depending on the latitude and the direction of the geostrophic wind. At 45° latitude, differences of 6 and 30% are noted in the drag coefficient and the shear angle, respectively, owing to the variation of the wind direction alone. Asymptotic similarity theory and a higher-order correction are first tested for the range of low Reynolds numbers simulated, and then used to predict the friction velocity and stress direction at the surface for flows at arbitrary Reynolds number. A model for the variation of these quantities with latitude and wind angle is also proposed which gives an acceptable fit to the simulation results. No large-scale longitudinal vortices are found in the velocity fields, reinforcing the conjecture that unstable thermal stratification, in addition to inflectional instability, is required to produce and maintain the large-scale rolls observed in the Earth's boundary layer. Comparisons of the Ekman layer with a related three-dimensional boundary layer reveal similarities of the mean profiles, as well as qualitative differences.

1. Introduction

This paper is concerned with the turbulent Ekman layer. Specifically, we examine the turbulent state of an incompressible viscous fluid over a smooth flat surface, driven by a uniform pressure gradient while experiencing steady system rotation. This flow is a statistically stationary archetype of the planetary boundary layer (PBL) in the limit of neutral stratification, and the results provide information concerning models, or parameterizations, of the PBL.

Our approach is to simulate numerically the unsteady three-dimensional details of the turbulence; others who utilized this procedure for the Ekman layer include Deardorff (1970, 1972) and Mason & Thomson (1987). The present work differs from Deardorff and Mason & Thomson's in that all the significant scales of motion of the turbulent fields are computed by way of Direct Numerical Simulation (DNS). The previous studies employed Large Eddy Simulation (LES), a procedure in which the large scales are directly computed while the effect of the unresolved scales is approximated by a sub-grid scale (SGS) model. The advantage of LES over DNS is that higher-Reynolds-number flows may be simulated. However, since SGS models

introduce an unknown degree of arbitrariness, the 'clean' DNS fields can provide a more reliable basis for the study of flow physics. Moreover, it is possible to extrapolate certain DNS generated quantities to higher Reynolds numbers using theoretical arguments. For these reasons we chose the DNS approach.

Issues to be addressed using the DNS fields include (i) the presence or absence of large-scale coherent structures ('longitudinal' or 'roll' vortices) in neutrally stratified Ekman-layer turbulence, (ii) the effects of the horizontal component of the angular velocity vector (i.e. latitude) and (iii) implications for models of the PBL at high Reynolds number.

While roll vortices are an observed PBL phenomenon with important consequences for transport and therefore modelling (Le Mone 1973), the physics of their formation is uncertain. There is a question as to whether the rolls are the result of only the inflectional instability mechanism associated with the Ekman-layer profile, or also require the additional influence of buoyantly unstable motions. Deardorff (1972) found that only with an upward heat flux did eddies (represented by vertical velocity fields) become, if not rolls, at least distinctly elongated. Wippermann, Etling & Kirstein (1978) also found, using a linear theory with spatially dependent turbulent viscosity, that stable and unstable buoyancy profiles strongly damp and strongly amplify linear disturbances, respectively. Furthermore, although they were fully prepared to observe them, Mason & Thomson (1987) failed to find large-scale longitudinal vortices in their neutrally-stratified LES results. On the other hand, theories concerning PBL rolls based solely upon the inflectional mechanism have been proposed by Faller (1965) and Brown (1974). These theories have as their foundation the fact that, for certain Reynolds numbers, the Ekman layer contains longitudinal rolls in a quasi-laminar state. A distinction is made herein between strictly laminar flow (in which no disturbances are present), quasi-laminar flow (in which smooth secondary circulations exist) and fully turbulent flows (in which the fields are chaotic). The PBL rolls have been suggested to be the atmospheric counterparts of the quasi-laminar rolls observed under neutrally-stratified conditions in the laboratory (Faller 1963; Tatro & Mollo-Christensen 1967; Caldwell & Van Atta 1970). Whether or not these rolls survive as the Reynolds number is increased and the flow becomes turbulent is therefore the critical question in deciding between the two hypotheses. Etling & Wippermann (1975) have shown that linear disturbances may grow in the neutrally-stratified Ekman layer when the turbulence is modelled by a non-uniform eddy viscosity, although the impact of the eddy viscosity closure, as well as the fate of the linear disturbances once they enter the nonlinear regime, are unclear. This suggests that the coherence associated with the quasi-laminar roll might persist into the turbulent flow. Conversely, the absence of rolls in Mason & Thomson's LES results mentioned above would indicate that this is not the case. However, Mason & Thomson were forced to compromise on resolution to specify a domain large enough to support the rolls, should they exist. Because of this, and of the uncertainty in any LES introduced by the SGS model and 'wall function' surface boundary conditions, the DNS fields will provide useful new data concerning the issue of longitudinal vortices in neutrally stratified turbulence. Stratification effects will be included in future simulations.

Both Deardorff and Mason & Thomson investigated the influence of latitude on Ekman-layer turbulence, and drew opposite conclusions. Deardorff, who performed LES runs at a latitude of 45° north (with a west-northwesterly wind), found that the magnitude of the intercomponent turbulent kinetic energy transfer due to the system rotation is much smaller than the transfer produced by the pressure–strain

correlation. The inference was drawn that the primary effect of the latitude is to simply specify the value of the vertical rotation vector. This leads to the assumption that the '*f*-plane approximation', in which the horizontal component of rotation is neglected, applies to the turbulent Ekman layer, as well as to the nearly two-dimensional synoptic ('weather-map') scale flows for which it was originally developed. Mason & Thomson also performed an LES run at 45° latitude. They found results which, when compared to the case with no horizontal rotation vector (90° latitude), differed by 4% in the geostrophic drag coefficient u_*/G (where u_* is the friction velocity at the surface and G is the magnitude of the geostrophic wind) and 21% in the angle between the geostrophic wind and the surface shear stress. The apparent discrepancy can be resolved by realizing that system rotation is one of a number of 'extra strains' which have much greater influence on the turbulence than one would expect from the magnitude of the corresponding term of the energy budget (Bradshaw 1973). Streamline curvature, lateral divergence, bulk compression, longitudinal acceleration and buoyant forcing are other examples of such influences.

That the influence of the horizontal component of rotation might be important for turbulent flow is suggested by Etling & Wippermann (1975) and Leibovich & Lele's (1985) discovery of the strong dependence of linear growth rates on latitude. The horizontal component is found to both reduce the minimum Reynolds number at which disturbances first grow and to widen the band of unstable wavenumbers, compared to the case with only a vertical component of rotation. (A list of authors who have studied the linear stability of the latter, so-called 'traditional', problem is given in Leibovich & Lele.)

When latitude variation is considered, the direction of the geostrophic wind with respect to the (northward-pointing) horizontal component of the rotation vector also becomes a factor. Mason & Thomson's single 45° latitude LES was performed at conditions anticipated by linear theory to produce the maximum influence. We present below results of a systematic study of the wind direction–latitude effect from simulations at 45° latitude with the wind from each of the four points of the compass; results from simulations at other latitudes and wind headings are also discussed and used to infer more general behaviour.

Besides acting as a source of physical insight, we expect the DNS fields to be useful as an 'experimental database' providing diagnostic information for analytic theories and LES PBL codes run with neutral stratification at low Reynolds numbers. We further expect to use the results to extrapolate modelling information to high-Reynolds-number atmospheric flows over smooth surfaces. To perform this latter task, the asymptotic theory developed by Csanady (1967) and others and recently extended to higher order by Spalart (1989) will be used to provide the drag coefficient u_*/G and the angle between the geostrophic wind and the surface shear stress, β, as a function of Reynolds number. A simple model of the latitude–wind direction effect at arbitrary Reynolds number will also be proposed, and a procedure for including the influence of surface roughness in the model will be discussed.

An experimental study of the turbulent Ekman layer has been performed by Caldwell, Van Atta & Helland (1972) using a rotating table apparatus. They were able to match much of the atmospheric field data and Deardorff's LES results, despite the complications caused by finite radius effects associated with the rotating table. Experimental and DNS velocity profiles will be compared below.

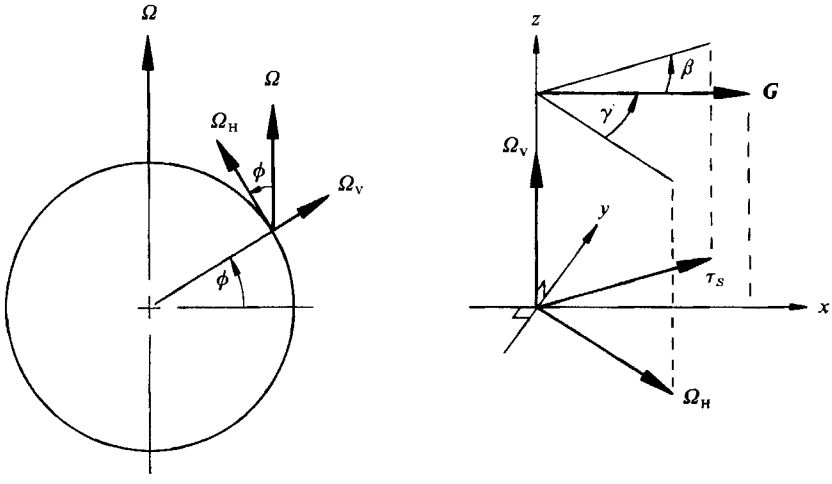

FIGURE 1. Coordinate system and parameter definition.

2. Problem formulation

The equations to be solved, over the domain $-\infty \leqslant x \leqslant \infty, -\infty \leqslant y \leqslant \infty, 0 \leqslant z \leqslant \infty$, are those which govern the flow of an incompressible viscous fluid in a rotating reference frame:

$$\frac{\partial \boldsymbol{u}}{\partial t} + \boldsymbol{u}\cdot\nabla\boldsymbol{u} = -\frac{1}{\rho}\nabla p + 2\boldsymbol{\Omega}\times(\boldsymbol{G}-\boldsymbol{u}) + \nu\nabla^2\boldsymbol{u}, \tag{1}$$

$$\nabla\cdot\boldsymbol{u} = 0. \tag{2}$$

$\boldsymbol{\Omega}$ is the angular velocity of the system, with vertical and horizontal components Ω_V and Ω_H, respectively, and $\boldsymbol{G}$ is the geostrophic wind which defines, along with the acceleration of gravity $\boldsymbol{g}$, the imposed uniform pressure gradient via

$$\nabla P = -2\rho\boldsymbol{\Omega}\times\boldsymbol{G} + \rho\boldsymbol{g}. \tag{3}$$

p is the deviation of the pressure from the imposed field given by (3), $\boldsymbol{u}$ the velocity vector, ρ the fluid density and ν the kinematic viscosity. Equations (1) and (2) are to be solved subject to the boundary conditions

$$\boldsymbol{u} = 0 \quad \text{at } z = 0, \quad \boldsymbol{u} \to \boldsymbol{G} \quad \text{as } z \to \infty. \tag{4}$$

At times sufficiently long, so that the turbulence 'forgets' the initial conditions and reaches a statistically stationary state, the quantities which uniquely specify the flow are the freestream geostrophic wind, $\boldsymbol{G}$, the rotation vector, $\boldsymbol{\Omega}$, and the kinematic viscosity of the fluid, ν. An appropriate set of non-dimensional parameters can therefore be chosen which includes the latitude, ϕ, the angle, γ, between Ω_H and $\boldsymbol{G}$, and a Reynolds number,

$$Re \equiv \frac{G}{(\frac{1}{2}\nu f)^{\frac{1}{2}}}$$

where $f \equiv 2\Omega_V = 2\Omega\sin\phi$ is the Coriolis parameter, and G is the geostrophic wind speed. Re was designed for laminar flow, which exactly satisfies the f-plane approximation; this motivates the use of f instead of Ω. The geometric relationships among $\Omega_V, \Omega_H, \phi, G$, and γ, as well as the system coordinates, are shown in figure 1.

The velocity and lengthscales which define the Reynolds number are G and the viscous depth $D \equiv (2\nu/f)^{\frac{1}{2}}$; alternative, 'inherent', velocity and lengthscales are the

friction velocity at the surface, u_*, and the turbulent depth, $\delta \equiv u_*/f$. While either set of scales may be used for the non-dimensionalization of the results shown below, the latter set leads to a more Reynolds-number independent presentation when the flow is turbulent, and is adopted (Tennekes 1982).

3. Numerical implementation

The weighted-residual method developed by Spalart (1986*a*) is used to generate the turbulent fields. The technique utilizes basis functions which are periodic in the homogeneous x- and y-directions and, vertically, are expansions in terms of Jacobi polynomials in the variable $\zeta = \exp(-z/Z)$ (where Z is the lengthscale of the associated mapping). The Fourier–Jacobi basis functions are constructed so that the velocity field automatically satisfies the continuity equation (2) and boundary conditions (4), resulting in good computational efficiency: an initial-value, rather than initial-boundary-value, problem in only two dependent variables is solved. The pressure field need not be computed as part of the solution for the velocity field, with p implicitly assumed to vary periodically in the x- and y-directions. The basis functions also include a term to exactly resolve the slowly-decaying irrotational velocity fluctuations, which allows the vertical grid points to be clustered in the highly vortical region near the surface, without compromising the accuracy of the calculation in the outer flow. Further, the structure of the basis functions leads to matrices that are narrow-banded, an attribute which is exploited to reduce the cost of the computation. The single most expensive part of the code is the 'Jacobi transform', involving typically 40% of the calculation; the operation count at each timestep for this procedure is $\frac{128}{27} N_x \cdot N_y \cdot N_z^2$, where N_x, N_y and N_z are the number of grid points in the x-, y- and z-directions. A mixed explicit–implicit time advance algorithm is used, with the timestep determined by the stability limit of the explicit scheme (which is applied to the nonlinear and Coriolis terms). To increase the size of the allowable step, the integration is performed in a translating Galilean reference frame moving in the direction, and at half the speed, of the freestream geostrophic velocity. While mass is conserved exactly, there is no special attempt made to discretely conserve momentum or energy. The total method is spectrally accurate (that is, the numerical error approaches zero faster than any power of the grid spacing as the resolution is increased) in all three spatial directions and second-order accurate in time; further details are available in Spalart (1986*a*).

Initial conditions for the simulations consist of small or moderate level random disturbances (as large as 3% of the freestream velocity in each component) at all resolved wavelengths, superimposed on the laminar Ekman-layer profile. When available, an existing turbulent field is used for the initialization. To speed up the development of a mature stationary state, two procedures are employed. The first is the execution of the early portions of a run on a coarse grid until the turbulent spectrum 'fills up' and a balance is reached among the steady-state terms of the Reynolds-averaged momentum equation. The second is the time advancement of the mean (zero wavenumber) variables with a 'virtual' timestep up to ten times larger than that appropriate for the fluctuations. The effect of this over-relaxation of the (spatial) mean is to accelerate the decay of any temporal oscillations of the zero-mode profile at the inertial frequency, as well as to hasten the arrival of the equilibrium state (Spalart 1989).

Once the coarse-grid steady-state balance is achieved the fields are regridded, so that they become fully resolved, and advanced in time. Transients produced by the

regridding are allowed to decay, after which averages in time of the velocity field are taken at intervals of approximately $tf = 0.02$. The 'means' presented below are the result of averaging over both time and the homogeneous directions of the flow. This implies that correlations are actually time averages of the deviation from the instantaneous spatial average, rather than from the final time and space averages.

Although there is no compelling reason to presume that the inertial timescale is relevant to turbulence physics, it is possible that the spatial mean flow will contain a residual oscillation with period $2\pi/f$, and influence the turbulence indirectly. Consequently, time averages are taken over a sample containing at least one inertial period. The adequacy of this precaution will be discussed further below. In all cases, the averaging procedure is continued until the mean profiles satisfy the steady-state Reynolds-averaged momentum equation to the extent that the integral of the mean velocity defect is within at least 2% of the equilibrium value.

To verify the reliability of the program, the growth rates and phase speeds of instabilities in the laminar Ekman layer were computed. The properties of the most unstable mode at four different Reynolds numbers matched the numerical findings of Melander (1983), Leibovich & Lele (1985) and Lele (private communication) to at least three significant figures. This agreement, together with tests performed by Spalart (1986*a*) and success in simulating boundary-layer flows (Spalart 1988) provide confidence in the results.

4. Cases

4.1. *Physical parameters*

Fifteen separate turbulent cases are examined, all but one at Reynolds number 400; the physical parameters for each case are shown in table 1. The notation relates the cases to the corresponding meteorological flow in the Northern Hemisphere, where the number denotes the latitude and the letter the direction from which the wind originates: west, east, north, or south. The highest Reynolds number case is B90, with $Re = 500$. The A-series allows a study of the influence of latitude and wind direction as well as, in conjunction with B90, a measure of the effect of Reynolds number. C90, D90 and E90 are coarse-grid cases, with the same physical parameters as A90, used to investigate numerical issues. A quasi-laminar reference case at $Re = 150$, 'R90', is also computed.

4.2. *Numerical parameters*

The horizontal lengths of the numerical domain, L_x and L_y, are each specified to be approximately twice the turbulent depth, δ. A sufficiency check on this condition was made by computing the horizontal two-point correlations, and by running cases C90 and D90. The latter cases differed from each other only in the size of the horizontal domains: D90 used $2\delta \times 2\delta$,C90, $4\delta \times 4\delta$. Details of the comparison will be discussed below. The location of the highest vertical quadrature point is at least $z = 1.6\delta$. Vertical profiles of mean velocity, Reynolds stresses and r.m.s. vorticity shown below indicate that this value is reasonable.

The spatial resolution used was guided by previous DNS of two- and three-dimensional boundary layers (Spalart 1988, 1989). Enough collocation points are utilized in the A and B series runs so that the horizontal grid spacing is less than 8 viscous units, i.e. $\Delta x^+ \equiv u_* \Delta x/\nu \leqslant 8$. Horizontal energy spectra were monitored to verify the validity of this criterion. In the vertical direction, the first grid point above the surface is at $z^+ \approx 0.2$ and the first ten points are within approximately $z^+ = 10$.

Case	Re	ϕ (deg.)	γ (deg.)
A90	400	90	—
A45W	400	45	270
A45E	400	45	90
A45N	400	45	180
A45S	400	45	0
A30E	400	30	90
A25W	400	25	270
A15W	400	15	270
A10E	400	10	90
A05W	400	5	270
A00E	400	0.1	90
B90	500	90	—
C90	400	90	—
D90	400	90	—
E90	400	90	—
R90	150	90	—

TABLE 1. Physical parameters

Case	N_x	N_y	N_z	L_x/δ	L_y/δ	Z/δ	z_{max}/δ	Δx^+	Δy^+
A90	96	96	45	2.0	2.0	0.25	1.8	7	7
A45W	96	96	45	2.1	2.1	0.26	1.9	7	7
A45E	96	96	45	2.0	2.0	0.25	1.8	7	7
A45N	96	96	45	2.0	2.0	0.25	1.8	7	7
A45S	96	96	45	2.0	2.0	0.25	1.8	7	7
A30E	96	96	45	1.9	1.9	0.24	1.7	8	8
A25W	96	96	45	2.1	2.1	0.27	1.9	7	7
A15W	96	96	45	2.2	2.2	0.27	2.0	7	7
A10E	96	96	45	1.8	1.8	0.22	1.6	8	8
A05W	96	96	45	—	—	—	—	—	—
A00E	96	96	45	—	—	—	—	—	—
B90	128	128	50	2.1	2.1	0.26	2.0	8	8
C90	96	96	35	3.9	3.9	0.24	1.6	15	15
D90	48	48	35	2.0	2.0	0.24	1.6	15	15
E90	48	48	35	2.0	2.0	0.24	1.6	15	15
R90	2	32	30	—	—	—	—	—	—

TABLE 2. Numerical parameters

The vertical lengthscale, Z, used in the exponential mapping to achieve this resolution is typically $\frac{1}{4}\delta$. The number of grid points, as well as the value of the other numerical parameters used for each of the cases is listed in table 2. As a result of the dealiasing procedure employed, the number of spectral modes in each direction is $\frac{2}{3}$ the number of grid points (Spalart 1986*a*).

The R90 reference case uses only enough grid points to resolve the quasi-laminar flow structure, which depends on only two spatial variables; the domain is configured to support the most linearly unstable wave at this Re. The vertical lengthscale used is twice the viscous depth: $Z = 2D$.

Runs were made on the NASA-Ames Cray XMP with the fully resolved $Re = 400$ and 500 cases requiring 8 and 15 CPU seconds per step, respectively. The code completed about 6000 timesteps in advancing an inertial time period, which

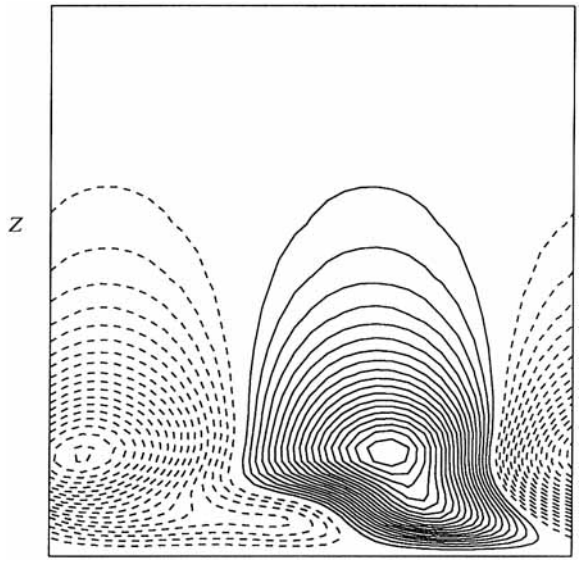

FIGURE 2. Contours of vertical velocity, w/G, in a vertical plane normal to the axis of longitudinal rolls in $Re = 150$ quasi-laminar flow at 90° latitude. ——, $w/G > 0$; – – –, $w/G < 0$; contour interval 0.001. The height and width of the region shown are $13D$ and $12D$, respectively. Angle between roll axis and geostrophic wind is 11°.

translates to an average step size of about $\Delta tf = 0.001, \Delta t^+ \equiv (u_*^2/\nu)\,\Delta t = 0.4$, or $(G/\delta)\,\Delta t = 0.015$.

5. Results

5.1. *90° latitude* ($\Omega_H = 0$)

A quasi-laminar reference case at $Re = 150$ was first computed. Vertical velocity contours in the vertical plane normal to the axis of the resultant roll cells (not the geostrophic wind) are shown in figure 2. The view shown is looking along the roll axis, roughly downstream. This field, which varies in only two spatial dimensions, was produced using initial conditions consisting of a single disturbance, corresponding to the linearly most unstable wave, superimposed upon the laminar profile. The amplitude of the wave reached a steady finite value. The angle between the freestream velocity and the surface shear stress for this flow is 43.9°, not appreciably different from the laminar 45° value. This indicates that the Reynolds stress induced by the wave is quite weak at $Re = 150$.

Repeating the single wave initialization at $Re = 400$ produces a flow in which the strength of the roll cell is not steady, as with $Re = 150$, but instead varies periodically in time. Since the field is constrained by the initialization to remain quasi-laminar (in particular, no variation in space in the direction parallel to the roll axis is allowed) at a Reynolds number large enough to sustain turbulence, the resulting state is somewhat artificial and not reported in detail here. When low-level three-dimensional disturbances (0.01% of freestream in each component) are superimposed on this pulsing, quasi-laminar field, the flow quickly breaks down and soon resembles the turbulent cases discussed below.

Contours of vorticity magnitude from a realization of the turbulent flow calculated as part of the $Re = 400$ A90 series are shown in figure 3. The view is of the full computational domain. The freestream flow is from left to right, into the plane of the

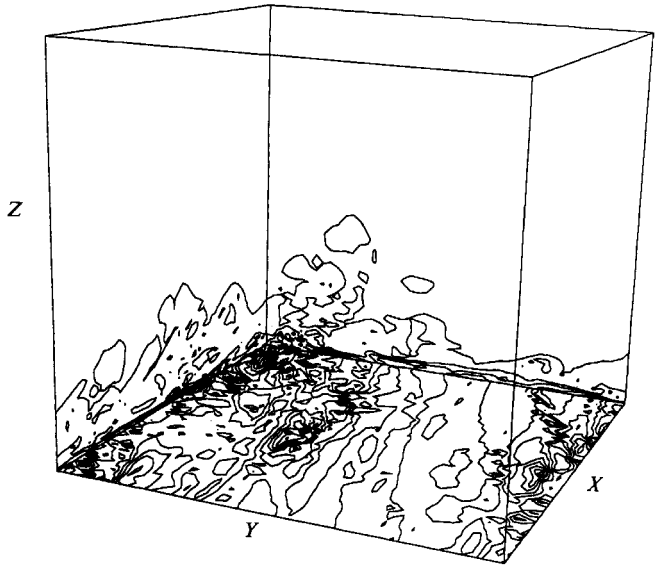

FIGURE 3. Contours of vorticity magnitude, $|\omega|D/G$, on the sides and bottom of the domain for a realization of case A90 $Re = 400$ turbulent flow at 90° latitude. The minimum contour level is 0.15, the contour interval 0.5, with a maximum value 5.47 observed.

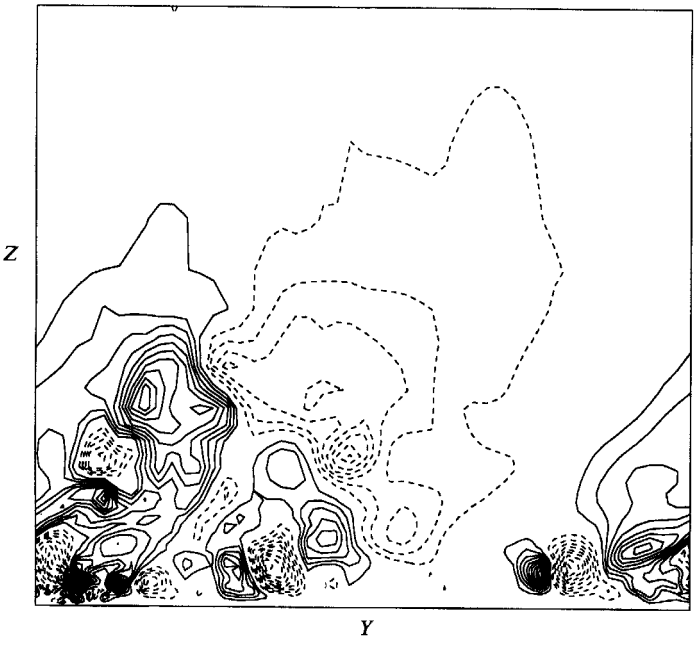

FIGURE 4. Contours of vertical velocity, w/G, in a vertical plane normal to the geostrophic wind for a realization of case A90 $Re = 400$ turbulent flow at 90° latitude. ——, $w/G > 0$; – – –, $W/G < 0$; contour interval 0.012, with observed extreme values of -0.14 and 0.17. View looking downstream.

paper, and only the left-hand (streamwise), downstream (spanwise), and lower surfaces contain curves. Figure 4 is the turbulent equivalent of figure 2, displaying instantaneous contours of vertical velocity in a vertical plane normal to the geostrophic wind. These figures illustrate the turbulent character of the solutions.

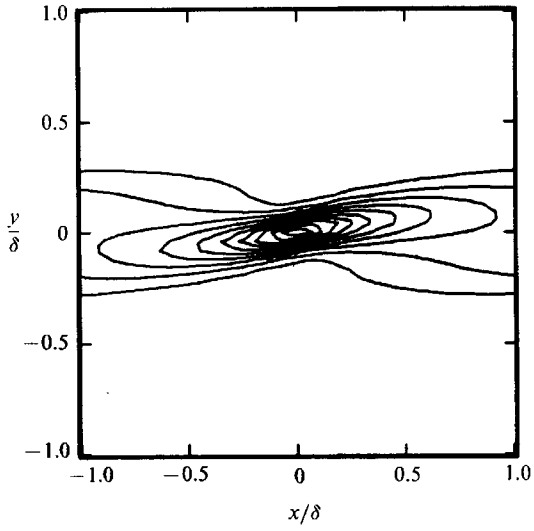

FIGURE 5. Contours of two-point velocity correlation coefficient R_{ii} (summed over all three components) on horizontal plane at $z/\delta = 0.03$ ($z^+ = 9$) for case A90 ($Re = 400$). ——, $R_{ii} \geqslant 0$; contour interval 0.1.

Two-point correlations

Two-point velocity correlations (summed over all three components) on horizontal planes for case A90 ($Re = 400$) are displayed in figures 5–7, with the freestream geostrophic wind aligned with the x-axis (see figure 1). Figure 5 corresponds to the horizontal plane at $z = 0.03\delta$ ($z^+ = 9$) which is near the location of maximum turbulent kinetic energy production. The correlation and one realization of the instantaneous u, v and w velocity fields at $z = 0.2\delta$ are shown in figure 6(a–d); correlation data from $z = 0.3\delta$ are given in figure 7. The turning of the mean velocity gradient vector with height induces the change in direction of maximum coherence observed in the figures. The fields also become more isotropic with increasing z. The correlations are similar to those of Mason & Thomson, and indicate the absence of coherent roll vortices. If rolls were present, the high contour levels would be much more elongated in the x-direction. The correlation field associated with the quasi-laminar flow of figure 2 consists of straight contours parallel to the roll axis. A purely isotropic field would produce circular contours. While the contour plots indicate some streamwise stretching of eddies by the mean velocity gradient, the low level associated with a separation equal to $\frac{1}{2}L_x$ demonstrates that the turbulent field is very different from the quasi-laminar flow shown in figure 2.

Since the 0.2 contour is not closed within the domain at $z/\delta = 0.2$, the correlation fields indicate that the $2\delta \times 2\delta$ box size is only marginally adequate. Adding to this concern is the fact that the range of linearly unstable waves (in the laminar flow) has been shown to be very wide, extending to lengths much larger than the lateral dimension of the computational domain (Leibovich & Lele 1985). It is thus conceivable that the A90 results are not independent of the numerical domain, an unacceptable situation. To investigate this question, the linear stability analysis was repeated for $Re = 400$ using Leibovich & Lele's code with, instead of the laminar Ekman profile, the modified mean of case A90 as the background state. (The molecular viscosity was retained.) The growth rates were greatly reduced in general, although modes at some angles were found to remain unstable. A more telling test

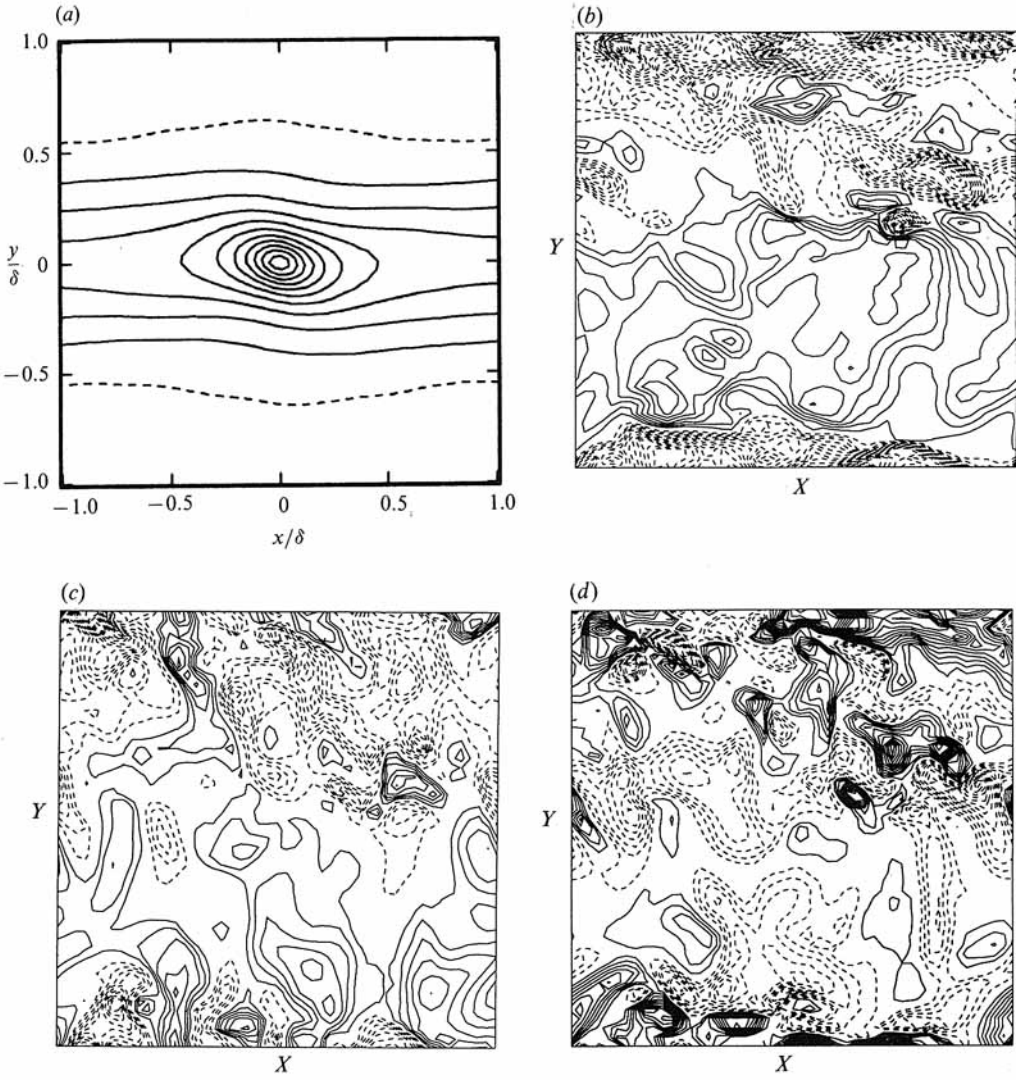

FIGURE 6. Contours of (*a*) two-point velocity correlation coefficient R_{ii} (summed over all three components), and instantaneous, (*b*) u/G, (*c*) v/G, and (*d*) w/G velocity components (with mean removed) on horizontal plane at $z/\delta = 0.2$ ($z^+ = 70$) for case A90 ($Re = 400$). (*a*) ——, $R_{ii} \geqslant 0$; – – –, $R_{ii} < 0$; contour interval 0.1 (*b*)–(*d*) Legend, contour interval, and (minimum, maximum) values: (*b*) ——, $u/G > 0$; – – –, $u/G < 0$; 0.02, (−0.40, 0.16). (*c*) ——, $v/G > 0$; – – –, $v/G < 0$; 0.02, (−0.27, 0.15). (*d*) ——, $w/G > 0$; – – –, $w/G < 0$; 0.012, (−0.16, 0.17).

of the influence of domain size on the results was performed by running cases C90 and D90 (which differ only in domain size, $4\delta \times 4\delta$ and $2\delta \times 2\delta$, respectively). The averaging time for the small domain run was four times as long as that for the large domain run, to ensure that the same number of samples entered the determination of the time–space means for both cases. Limited computer resources constrained the large (and therefore the small) domain run to use a coarse grid, resulting in slightly under-resolved fields. The correlation at $z = 0.2\delta$ from the large domain run is shown in figure 8. The D90 correlation at $z = 0.2\delta$ is similar to that for A90 given in figure 6(*a*). Comparing figures 6(*a*) and 8, in which the plot sizes are proportional to domain

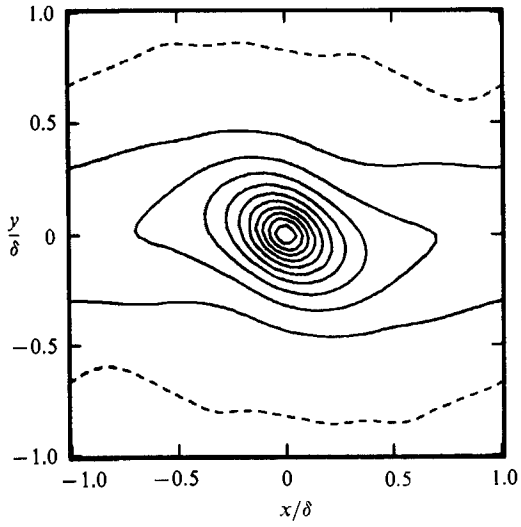

FIGURE 7. Contours of two-point velocity correlation coefficient R_{ii} (summed over all three components) on horizontal plane at $z/\delta = 0.3$ ($z^+ = 110$) for case A90 ($Re = 400$). ——, $R_{ii} \geqslant 0$; – – –, $R_{ii} < 0$; contour interval 0.1.

sizes, gives an indication of the effect of the box size on the correlation. The larger domain does indeed produce a significantly improved correlation field for large separations; however, while the box size for the two cases changes from marginal to very good, the friction velocity at the surface, u_*, and the angle of the surface shear stress with respect to the freestream velocity, β (figure 1), change by only 0.1 and 2%, respectively. The energy associated with any long-wavelength linearly unstable modes which may be unresolved is evidently negligible. It appears that the smaller box size is adequate. Note that even the large domain does not lead to the presence of longitudinal rolls.

It is also possible that the orientation of the domain with respect to the geostrophic wind could influence the numerical results. To ensure that this is not the case, run E90 was performed. E90 is identical to case D90 except that the domain is rotated 45° with respect to $\boldsymbol{G}$. Very little difference is noted between the results of the two cases; the correlation fields are very similar and the values of both u_* and β differ by only 0.2%. This implies that the results presented below contain no directional bias introduced by the numerical procedure.

Global quantities

The time histories of the surface quantities u_* and β for run A90 are shown in figure 9. Since the values are derived from spatial means (averages over the domain), the oscillations in time have no direct physical significance. If the size of the box from which the spatial means are obtained were infinite, and the flow were statistically stationary, no time variation of the spatial mean would exist. While performing the small- and large-domain D90/C90 comparison runs discussed above (the former includes four times as many samples in the spatial mean as does the latter) the r.m.s. levels of the time signals were observed to be in a nearly two-to-one ratio, indicating that the oscillations in time of the spatial means are of a statistical nature (i.e. the r.m.s. scales with the inverse square root of the sample).

The time signals of the histories of the global quantities were Fourier decomposed

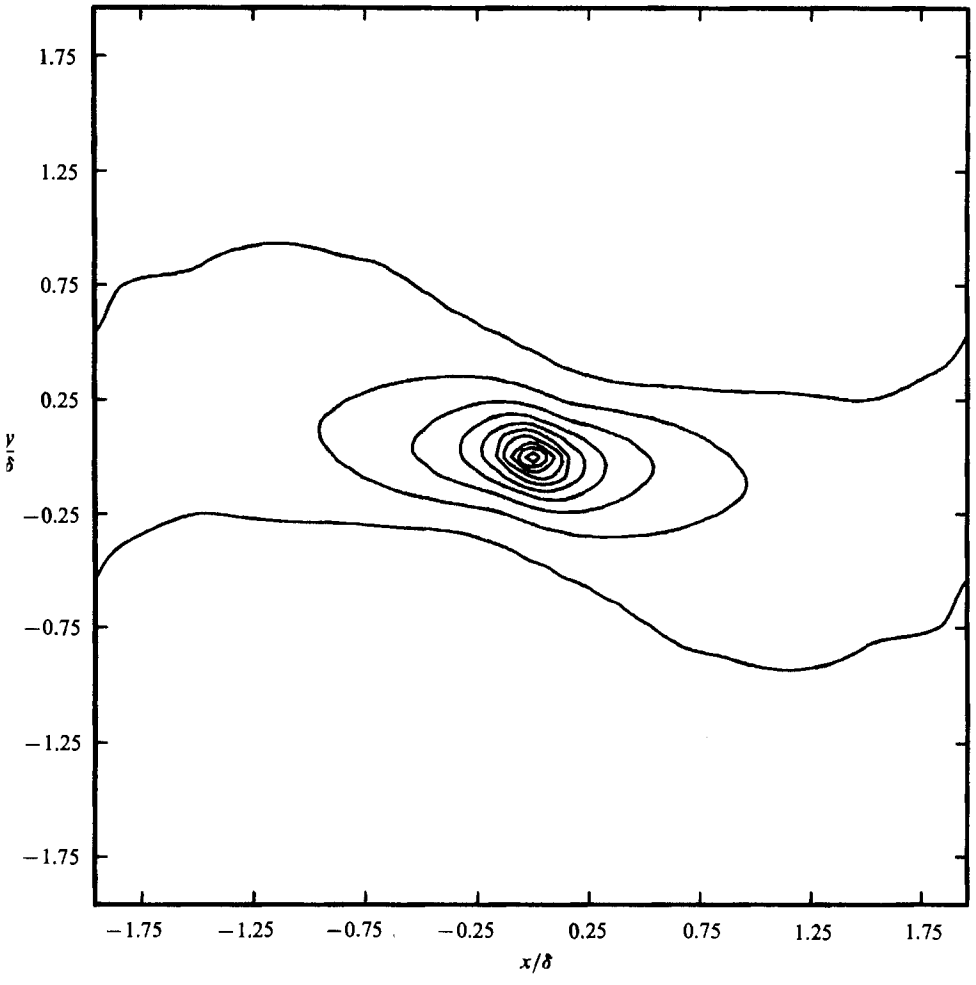

FIGURE 8. Contours of two-point velocity correlation coefficient R_{ii} (summed over all three components) on horizontal plane at $z/\delta = 0.2$ for case C90. ——, $R_{ii} \geqslant 0$; contour interval 0.1.

to see if dominant oscillations at the inertial frequency exist. None were observed. Samples containing as many as 20 inertial periods (cases D90 and E90) were analysed. The precaution of averaging over a period of exactly $tf = 2\pi$ (or a multiple) is therefore unnecessary. The lack of significant inertial-frequency oscillations leads us to conclude that, at least as far as the surface quantities are concerned, the flow is indeed in a stationary state.

Global results from all cases are given in table 3. Possible sources of error in the values given include both numerical (finite box size and space/time resolution) and statistical (finite time sample) inaccuracies. By appealing to studies performed by Spalart (1988, as part of a DNS investigation of two-dimensional boundary layers) of the influence of box size and grid spacing on the behaviour of the surface stress, we may estimate the likely numerical error for the present results. An indication of the statistical error is the quality of the global momentum balance determined by integrating the mean velocity defect and comparing with the surface stress. All the

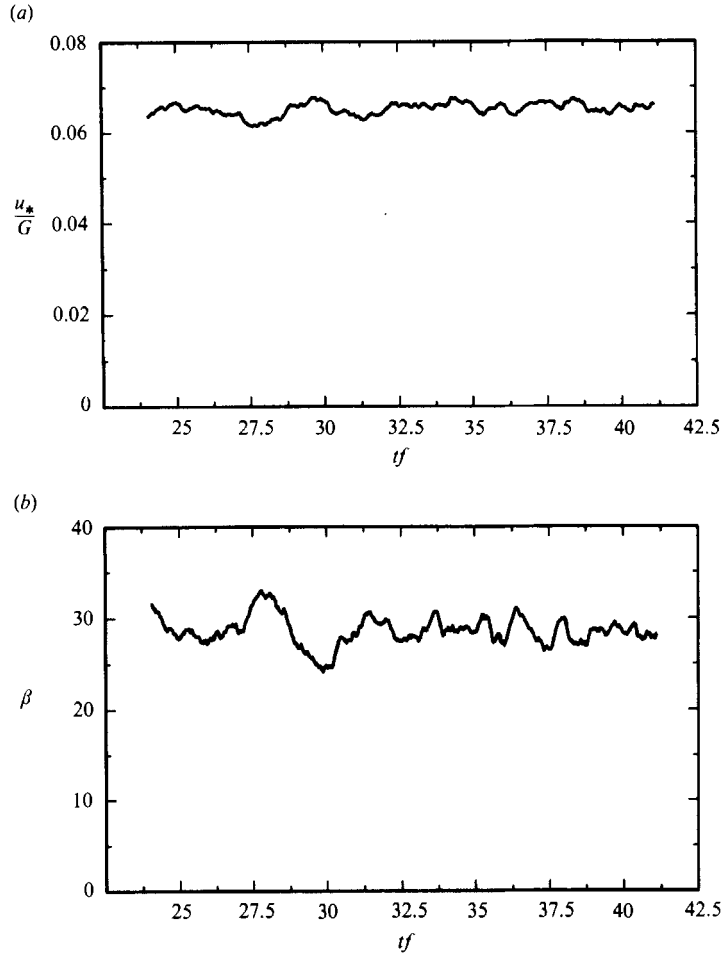

FIGURE 9. Time history of the spatial mean (*a*) friction velocity at the surface, u_*, and (*b*) angle between the geostrophic wind and surface shear stress, β, for case A90 ($Re = 400$).

table 3 values are computed from mean profiles that yield balances to within 2%. Most of the global momentum imbalance occurs in the outer flow region, where, because of the scale of the turbulence, the mean profiles tend to settle down more slowly. A quantitative measure of the statistical error is the difference of the partial averages of u_* and β taken over the first and second half of the time sample. From these considerations, we believe the maximum error in the values shown in table 3 is of the order of 1% for u_*/G and 3% for β.

Vertical profiles

Mean velocities from the $Re = 400$ series are exhibited in figure 10(*a*, *b*) in component and hodograph form. The component profiles indicate an Ekman-layer height, defined as the minimum height where $\langle \boldsymbol{u} \rangle$ and $\boldsymbol{G}$ are parallel ($\langle v \rangle = 0$), of about 0.7δ. The dotted curve hodograph in figure 10(*b*) represents the laminar solution. The same data, plotted in coordinates aligned with the surface shear stress are shown in figure 10(*c*) in inner (or viscous) units, in which velocities are normalized

Case	u_*/G	β (deg.)	δ/D
A90	0.0652	28.5	13.0
A45W	0.0625	34.2	12.5
A45E	0.0666	25.3	13.3
A45N	0.0652	28.5	13.0
A45S	0.0658	29.5	13.2
A30E	0.0689	23.4	13.8
A25W	0.0614	37.6	12.3
A15W	0.0600	42.1	12.0
A10E	0.0740	20.9	14.8
A05W	0.059	44.7	—
A00E	0.061	44.8	—
B90	0.0627	25.4	15.7
C90	0.0674	27.6	13.5
D90	0.0674	28.1	13.5
E90	0.0673	28.1	13.5
R90	0.097	43.9	

TABLE 3. Global results

by u_* and lengths by the viscous length ν/u_*. The logarithmic region at this Reynolds number is either very thin or non-existent.

The components of the velocity defect in shear stress coordinates, scaled by u_* and δ, are given in figure 11. With this scaling, the defect should be a universal function of z/δ in the outer region of the layer (Tennekes 1982). $Re = 400$ and 500 DNS results, A90 and B90, as well as the experimental results of Caldwell *et al.* (1972) are shown. The experimental velocity profiles yield global momentum balances which are far from equilibrium (as much as 40%); the discrepancy between the experimental data and the DNS is thought to be due mainly to finite radius effects inherent in the rotating table apparatus used in the laboratory. Within the inner layer, the components of the defect from the numerical results indicate the variation with Re of the magnitude and direction of the surface shear.

Root mean square fluctuations of the individual velocity and vorticity components from the ($Re = 400$) A90 series are displayed in figure 12, using both the inner and outer scalings. The magnitude of the vertical velocity component is smaller than its streamwise and spanwise counterparts throughout the boundary layer, except very near the top of the simulation domain (figure 12*a*). The small but finite velocity fluctuations at the top of the domain are due to the slowly decaying irrotational velocity field which is exactly resolved by the numerical method (see §3 and Spalart 1986*a*). The streamwise (freestream direction) fluctuations are the largest near the surface, but as the elevation increases they are reduced to a level less than, then equal to, that of the spanwise component. Except for this streamwise–spanwise reversal, which is a symptom of the three-dimensionality of the flow, the behaviour of the velocity perturbations is similar to that observed in two-dimensional boundary layers.

The rapid drop-off of the vorticity fluctuations with elevation (figure 12*b*), signifies that the height of the numerical domain is adequate. The spanwise component is largest throughout the layer. The profiles are again similar to their two-dimensional counterparts; note the large streamwise component near the surface,

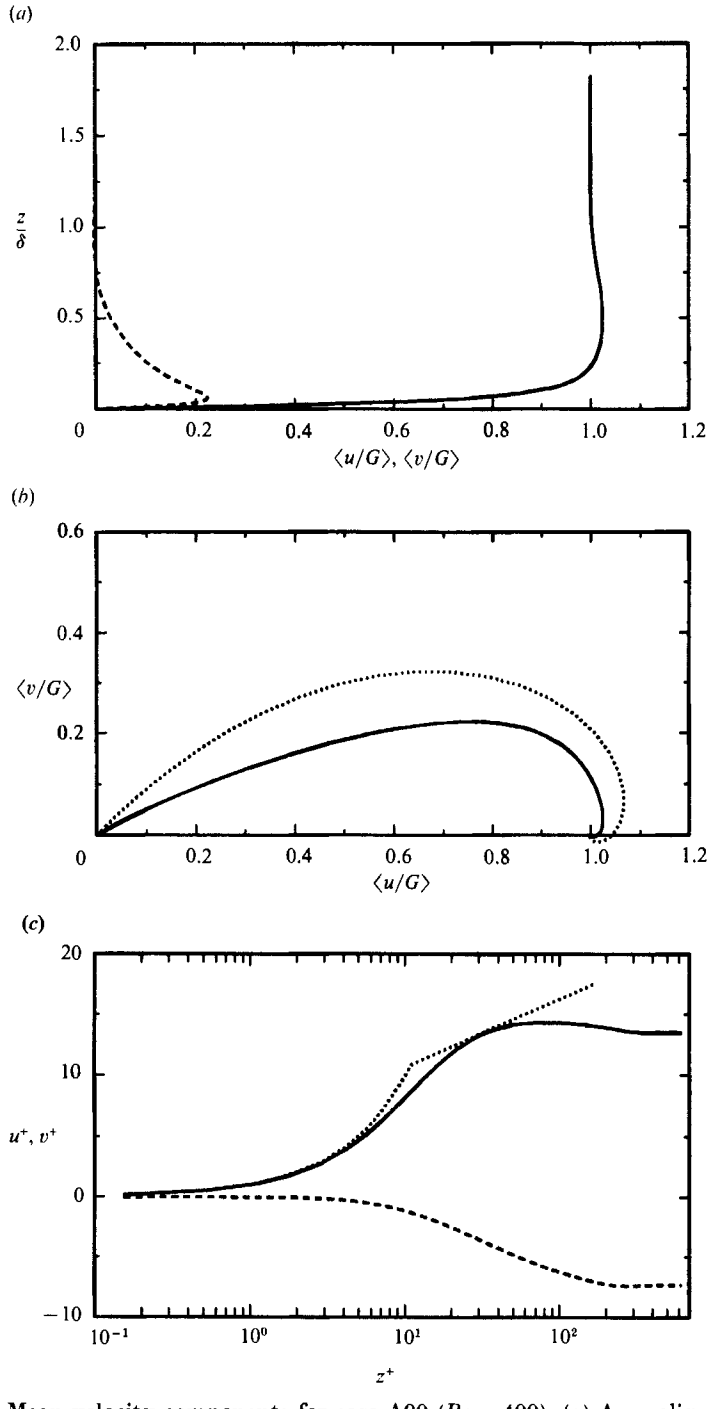

FIGURE 10. Mean velocity components for case A90 ($Re = 400$). (*a*) Axes aligned with freestream velocity; ——, streamwise; – – –, spanwise. (*b*) Hodograph. · · ·, laminar profile. (*c*) Axes aligned with surface shear stress; ——, shearwise; – – –, cross-shear; · · ·, $u^+ = z^+$ for $z^+ \leqslant 10, u^+ = \frac{1}{0.41} \ln z^+ + 5$ for $z^+ > 10$.

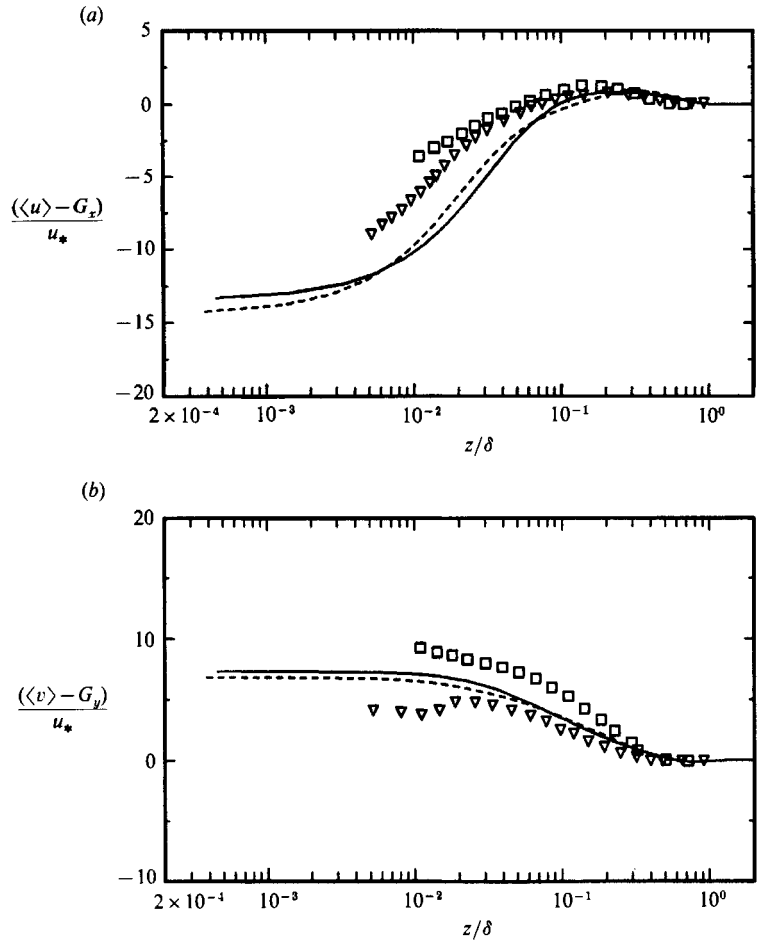

FIGURE 11. Mean velocity components, axes aligned with surface shear stress. (*a*) Shearwise defect. (*b*) Cross-shear defect. ——, case A90 ($Re = 400$); – – –, case B90 ($Re = 500$); □, Caldwell *et al.* (1972) run 1; ▽, Caldwell *et al.* (1972) run 7.

consistent with the characteristic near-wall 'streakiness' found in other boundary layers.

Total and Reynolds stress curves are shown in figure 13, in axes aligned with the freestream velocity, while figure 14 exhibits the variation of the direction of the Reynolds stress, velocity gradient and velocity vectors. All angles are measured with respect to the surface shear stress. The vertical coordinate here, and in the plots to follow, is limited to $z/\delta \leqslant 1$. Throughout the Ekman layer, the direction of the Reynolds stress and gradient vectors continues to spiral nearly linearly with z. From the surface up to an elevation of about $z = 0.1\delta$, the angle between the Reynolds stress and the surface stress is larger than that between the surface stress and the velocity gradient. Above $z = 0.1\delta$, however, the gradient angle is up to 30° larger than the stress angle. The significant differences in the direction of the shear and stress vectors imply that the use of an eddy viscosity closure, which assumes the Reynolds stress is aligned with the velocity gradient, is incorrect for this flow (despite this formal discrepancy, integration with an eddy viscosity model may produce mean velocities that are not in serious disagreement with actual profiles). Similar results for

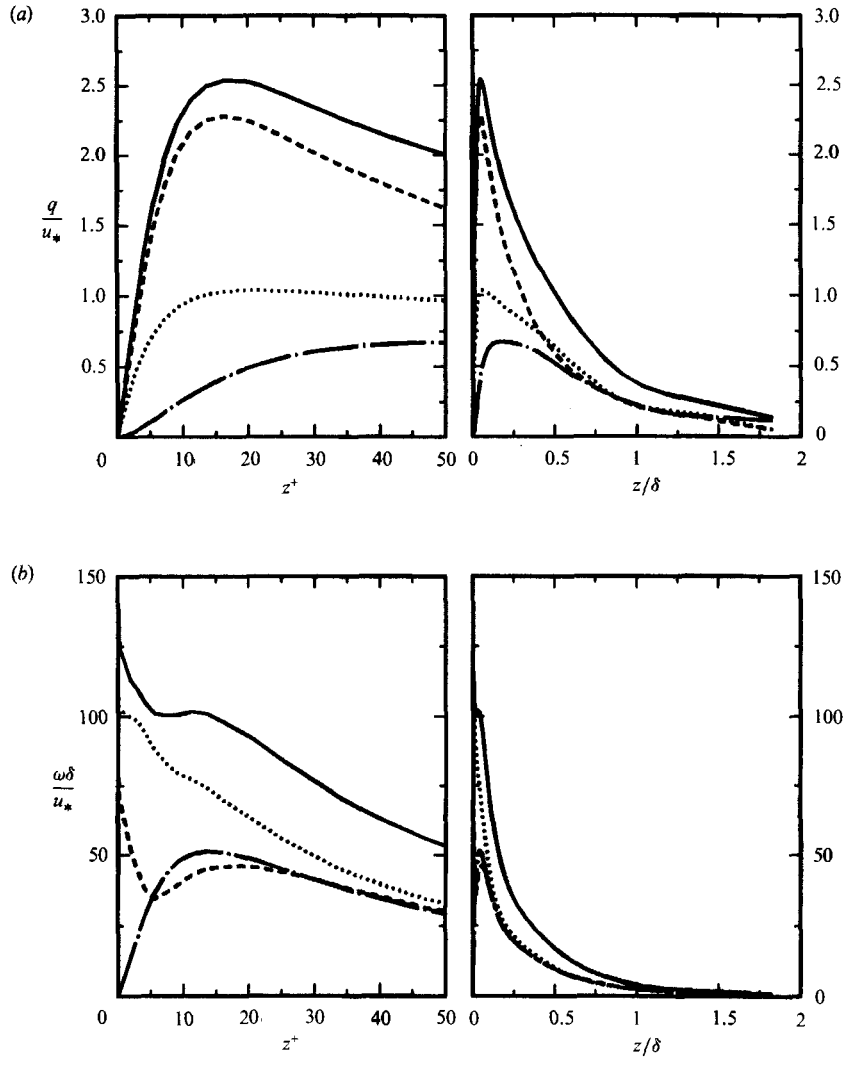

FIGURE 12. Root mean square fluctuations of (*a*) velocity, and (*b*) vorticity for case A90 ($Re = 400$). Axes aligned with freestream velocity; ——, total; – – –, streamwise; · · ·, spanwise; –·–, vertical.

the direction variation with height are presented by Deardorff (1970). However, because Deardorff's LES uses a surface-function lower-boundary condition, and the present DNS fully resolves the turbulence down to the no-slip surface, there is a difference. Unlike the situation shown in figure 14, the angles of the stress and gradient match at the bottom of the LES domain, and never cross. The relatively high location of the stress-gradient cross-over in the DNS flow is a consequence of the low Re. At Reynolds numbers typical of the PBL the cross-over presumably occurs at a much smaller value of z/δ.

The distribution with height of the magnitude of the eddy viscosity, ν_T, defined as either the ratio of the magnitude of the Reynolds stress to the magnitude of the velocity gradient, or the ratio of the turbulent kinetic energy production to the square of the magnitude of the velocity gradient, is shown in figure 15 (*a*) (the second

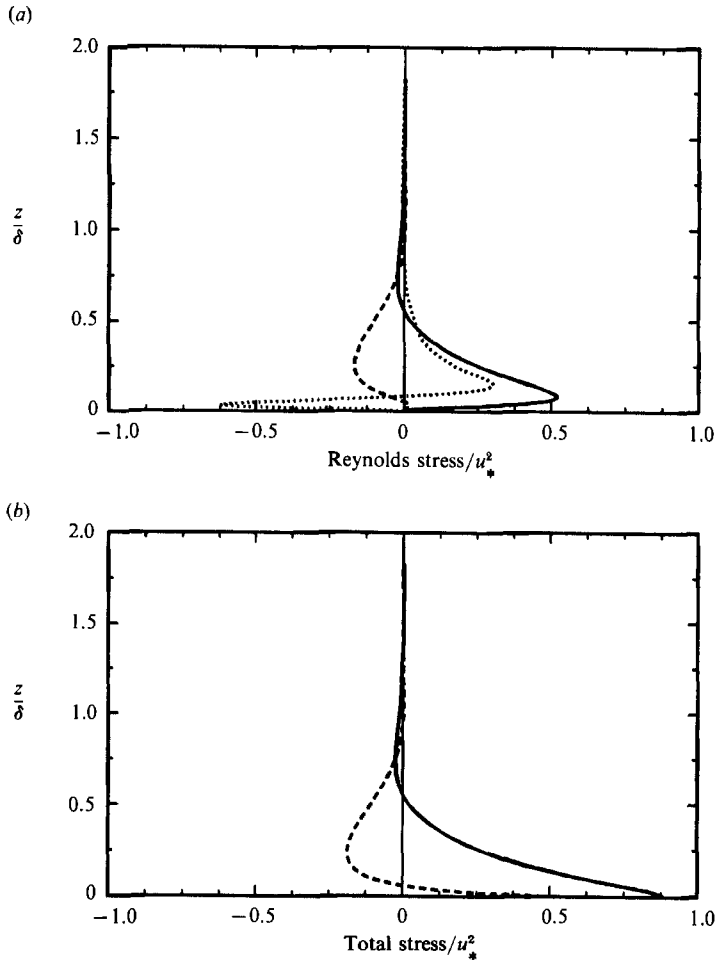

FIGURE 13. Stress profiles for case A90 ($Re = 400$) (axes aligned with freestream velocity). (*a*) Reynolds stress; ——, $-\langle uw \rangle$; – – –, $-\langle vw \rangle$; · · ·, $-\langle uv \rangle$. (*b*) Total stress; ——, streamwise; – – –, spanwise.

definition was suggested to us by Professor D. K. Lilly). The values of ν_T are comparable to those obtained by Deardorff (1970).

It is tempting to use a constant eddy viscosity when considering a turbulent flow in an effort to apply quasi-laminar Ekman-layer results to the turbulent case. However, the variation of the eddy viscosity with height demonstrated in figure 15(*a*), especially its reduction to zero near the surface, leads one to question the validity of such a practice. It has been shown that the quasi-laminar and turbulent flows differ qualitatively in that longitudinal rolls exist in one but not the other, and that the turbulent surface shear angle, β, is significantly less than the quasi-laminar value of nearly 45°.

Even formulations that use an eddy viscosity which varies with elevation may be of limited utility. For example, it is not clear that an analysis of wave-like disturbances in a turbulent flow, based on the turbulent mean profile and the 'exact' $\nu_T(z)$, would be meaningful. The reason is that the eddy viscosity contains contributions from the entire turbulent range of scales, which (unless the waves have

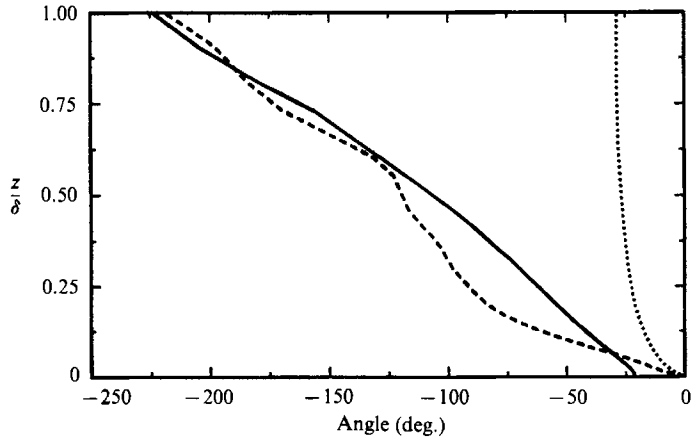

FIGURE 14. Direction of mean Reynolds stress, velocity gradient and velocity vectors, measured from surface shear stress (positive counterclockwise) for case A90 ($Re = 400$). ——, Reynolds stress; – – –, velocity gradient; · · ·, velocity.

lengthscales and timescales that are large compared with δ and $1/f$) includes the wavelength of interest.

Figure 15(*b*) presents the profile of the mixing length, l, the ratio of the square root of the magnitude of the Reynolds stress to the magnitude of the velocity gradient. The dashed line describes the curve $l = \kappa z$, with $\kappa = 0.41$. The mixing length is zero at the surface, grows rapidly and then more slowly with increasing z; the behaviour differs from the ideal constant stress layer in that $l/z \leqslant \kappa$ for the entire profile. This is thought to be a consequence of the favourable pressure gradient, since during a simulation of sink–flow boundary layers, the same behaviour was observed (see figure 9 of Spalart 1986*b*).

The vertical variation of the ratio of the magnitude of the Reynolds stress to the trace of the Reynolds stress tensor, known as the structure parameter, a_1, is given by the solid curve in figure 16. As with other three-dimensional boundary layers (Bradshaw & Pontikos 1985), the maximum value observed, 0.11, is less than the usual two-dimensional $a_1 \approx 0.16$. The other curves shown in figure 16 are results from cases with $\Omega_H \neq 0$, which will be discussed below.

Profiles of the mean velocity from run B90 ($Re = 500$) are given in figure 17(*a*, *b*). The component curves in figure 17(*a*) are similar to those from the $Re = 400$ case, figure 10(*a*), in that the cross-stream component crosses zero at approximately $z = 0.7\delta$. Significant differences exist in the hodograph representations, figures 10(*b*) and 17(*b*). A reduction of the angle between the freestream velocity and surface stress is observed in the higher-Reynolds-number flow, and the tops of the profiles are noticeably dissimilar.

The stress profiles in figure 18(*a*, *b*) reveal that the only major difference in the $Re = 400$ and $Re = 500$ results is in the behaviour of the uv-component (which, because of the homogeneity in x and y, does not enter into the Reynolds-averaged momentum equations). Figures 13(*a*) and 18(*a*) demonstrate that uw and vw are in near agreement, although at the higher Reynolds number they are slightly larger when scaled by u_*. The total stresses are in excellent agreement (figures 13*b* and 18*b*).

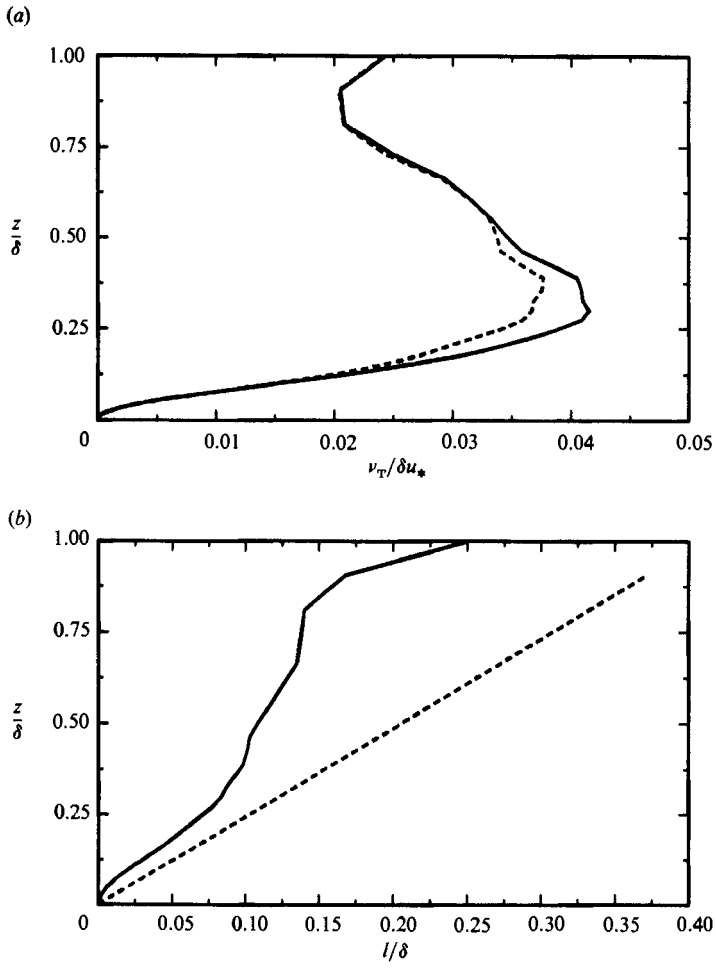

FIGURE 15. Eddy viscosity and mixing length profiles for case A90 ($Re = 400$). (*a*) Eddy viscosity.

$$\text{——}, (\langle uw\rangle^2 + \langle vw\rangle^2)^{\frac{1}{2}} \Big/ \left(\left(\frac{\mathrm{d}\langle u\rangle}{\mathrm{d}z}\right)^2 + \left(\frac{\mathrm{d}\langle v\rangle}{\mathrm{d}z}\right)^2\right)^{\frac{1}{2}};$$

$$\text{---}, \left(-\langle uw\rangle \frac{\mathrm{d}\langle u\rangle}{\mathrm{d}z} - \langle vw\rangle \frac{\mathrm{d}\langle v\rangle}{\mathrm{d}z}\right) \Big/ \left(\left(\frac{\mathrm{d}\langle u\rangle}{\mathrm{d}z}\right)^2 + \left(\frac{\mathrm{d}\langle v\rangle}{\mathrm{d}z}\right)^2\right).$$

(*b*) Mixing length.

$$\text{——}, (\langle uw\rangle^2 + \langle vw\rangle^2)^{\frac{1}{4}} \Big/ \left(\left(\frac{\mathrm{d}\langle u\rangle}{\mathrm{d}z}\right)^2 + \left(\frac{\mathrm{d}\langle v\rangle}{\mathrm{d}z}\right)^2\right)^{\frac{1}{2}}; \quad \text{---}, \kappa z, \text{ with } \kappa = 0.41.$$

5.2. *45° latitude* ($\Omega_H = \Omega_V$)

Time histories of u_* and β from the $\phi = 45°$ comparative wind direction runs at $Re = 400$ are exhibited in figure 19(*a–d*). As discussed above, the oscillations of these spatial mean quantities are statistical. On all plots, the solid line represents the $\Omega_H = 0$ run, A90, presented for reference. The largest difference occurs between the A45E and the A45W (east and west wind) results shown in figure 19(*a*, *b*). Figure 19(*c*, *d*) histories imply that the A45N and A45S north and south wind cases differ only slightly from the 90° latitude simulation.

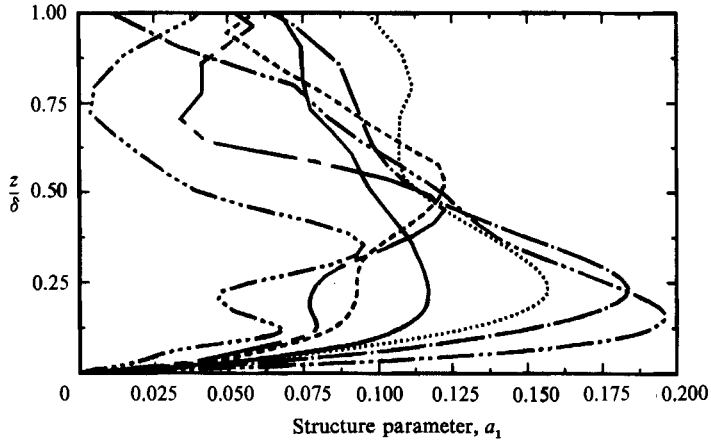

FIGURE 16. Structure parameter, a_1, from various latitude and wind direction cases at $Re = 400$. $a_1 = (\langle uw\rangle^2 + \langle vw\rangle^2)^{\frac{1}{2}}/(\langle u^2\rangle + \langle v^2\rangle + \langle w^2\rangle)$. ——, A90; – – –, A45W; – – –, A25W; – · · ·, A15W; · · ·, A45E; – · –, A30E; – · · –, A10E.

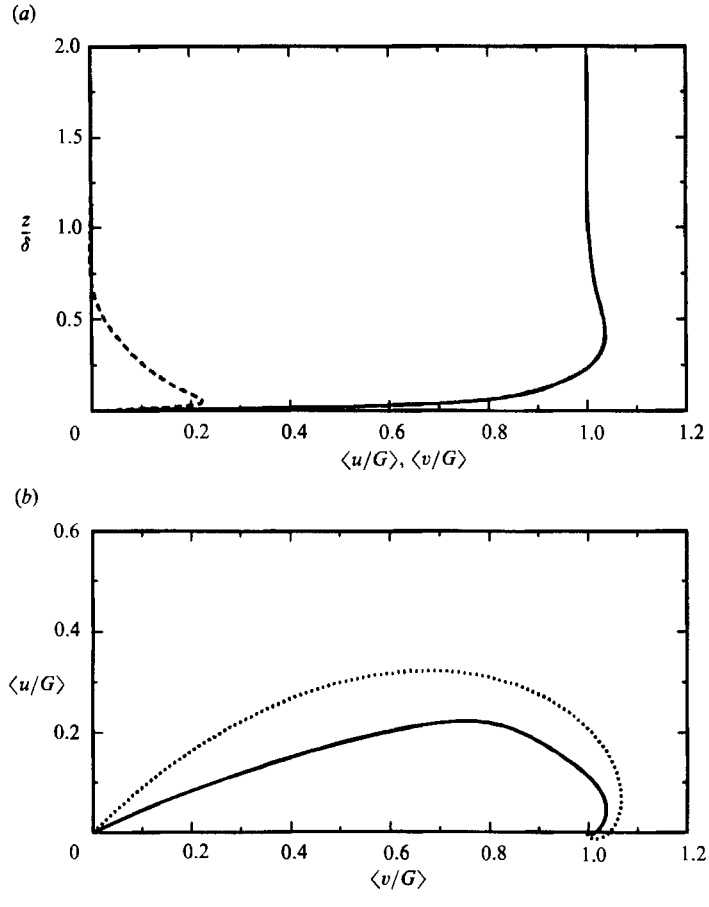

FIGURE 17. Mean velocity components for case B90 ($Re = 500$). (*a*) Axes aligned with freestream velocity. ——, streamwise; – – –, spanwise. (*b*) Hodograph. · · ·, laminar profile.

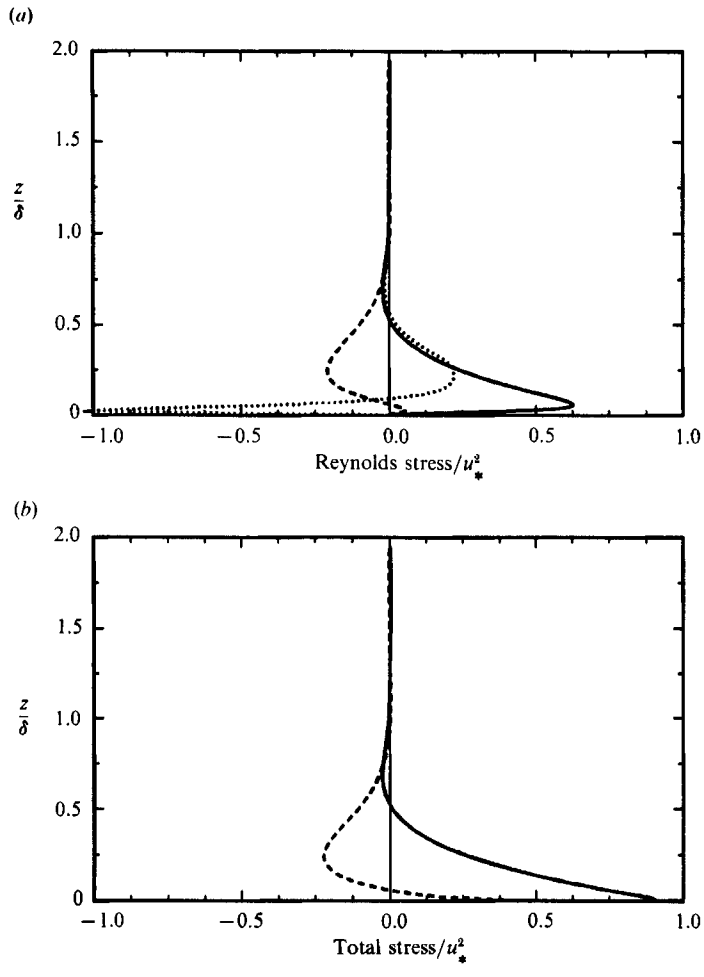

FIGURE 18. Stress profiles for case B90 ($Re = 500$) (axes aligned with freestream velocity). (*a*) Reynolds stress: ——, $-\langle uw\rangle$; – – –, $-\langle vw\rangle$; · · ·, $-\langle uv\rangle$. (*b*) Total stress: ——, streamwise; – – –, spanwise.

The variation with wind direction of time–space averaged values of the 45° latitude surface quantities is presented in figure 20(*a*, *b*). The plots show u_* and β as functions of the angle, γ, measured counterclockwise from the horizontal rotation vector Ω_H to the geostrophic wind (figure 1). The data points represent the DNS results, the horizontal line the results with $\Omega_H = 0$; the dashed curve is a least-squares interpolant of the form $c_1 + c_2 \cos\gamma + c_3 \sin\gamma$. The vertical scale of both plots has been expanded.

The latitude–wind direction effect is found to influence not just the surface stress behaviour, but also that of the structure parameter, a_1, through the depth of the layer. a_1 profiles from A90, A45E and A45W are shown in figure 16.

5.3. *Other latitudes* ($\Omega_H > \Omega_V$)

Figure 16 also contains structure parameter curves from the 'low latitude' A-series simulations A30E, A25W, A15W and A10E. (Since geostrophic winds from the north and south at $\phi = 45°$ led to flows little different from that at $\phi = 90°$, only east and

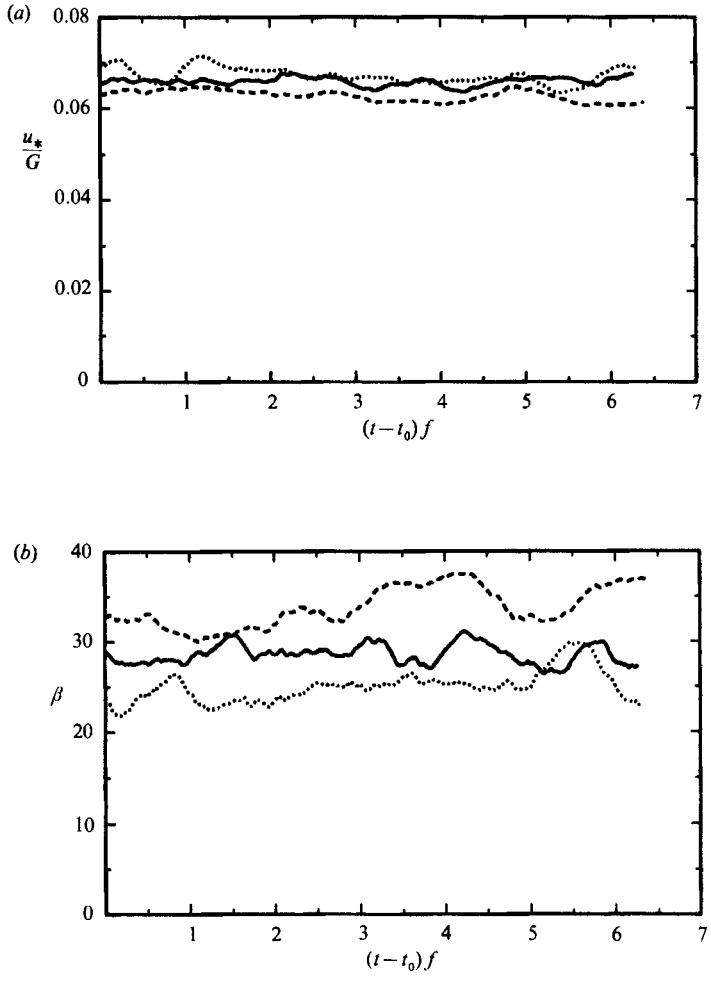

FIGURE 19(a, b). For caption see facing page.

west wind cases were computed.) Differences in the structure parameter are even more dramatic than those observed at $\phi = 45°$. Comparing all of the curves reveals a tendency for the maximum in the a_1 profile to increase as the latitude is reduced, when the wind is from the east. West wind results show the opposite effect as ϕ decreases, with the appearance of a double maximum in the profile.

The most severe reduction in a_1 (from A15W) is comparable to that in strongly three-dimensional boundary layers, where values as small as 0.09 have been found (Bradshaw & Pontikos 1985). This is interesting, since the Ekman layer is near equilibrium, while the strongly three-dimensional cases cited by Bradshaw & Pontikos are in a state of rapid adjustment to large cross-flow pressure gradients.

The surface stress results from these runs are shown in table 3. The east-wind cases are noted to become more 'turbulent', in the sense of higher u_*/G and lower β, as the latitude decreases, while the west-wind cases become less. This east/west enhancement/reduction trend continues with diminishing ϕ to the point that A10E is the most vigorous, and A15W the least vigorous, of the runs simulated. In fact, A15W is very weakly turbulent, associated with a near-laminar surface stress. At

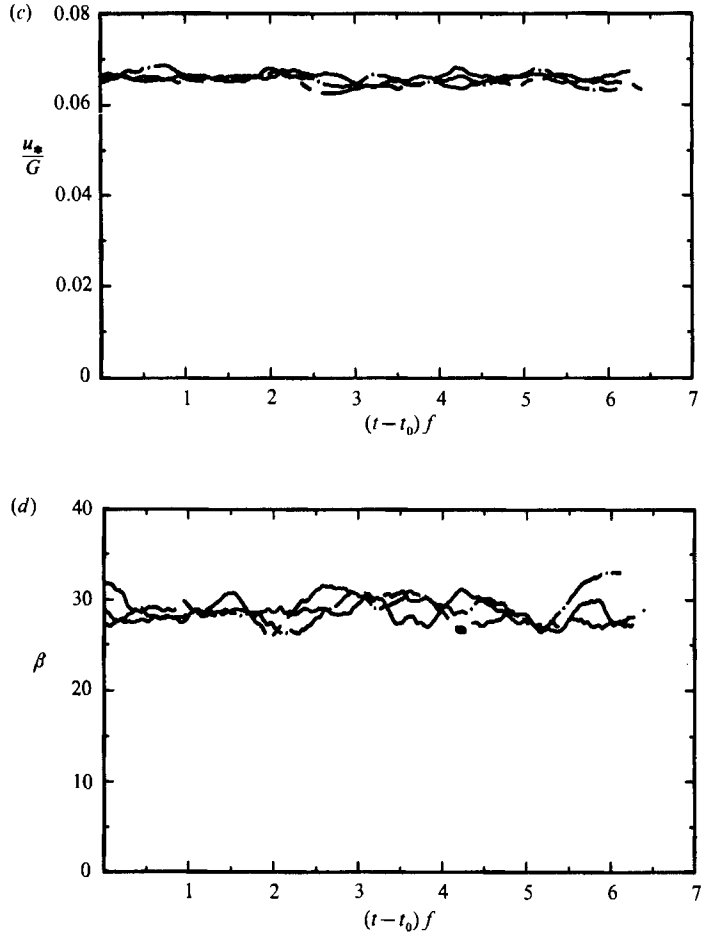

FIGURE 19. Time histories of the spatial mean (*a*), (*c*) friction velocity at the surface, u_*, and (*b*), (*d*) angle between the geostrophic wind and surface shear stress, β, for geostrophic winds with various orientations at 45° latitude with $Re = 400$. ——, A90; – – –, A45W; · · ·, A45E; – –, A45N; –·–, A45S.

very low latitudes, both east and west wind situations are similar, in that neither case A05W nor A00E ($\phi = 0.1°$) was able to sustain a turbulent state at $Re = 400$.

6. Discussion and conclusions

6.1. *Longitudinal rolls*

The linear instability which is the first stage of laminar to turbulent transition often leaves its mark on the turbulent field. A classic example is the Taylor–Couette flow in which vortex cells exist in both non-turbulent and turbulent flows. The Ekman layer could display similar behaviour. It was shown that, in the absence of noise, the linear instability can grow and saturate to produce a flow with a well-defined roll (see figure 2). However, when the initial conditions include disturbances to all resolved wavelengths, including those corresponding to the most unstable of the linearly unstable roll modes, the developed turbulent fields contain no evidence of

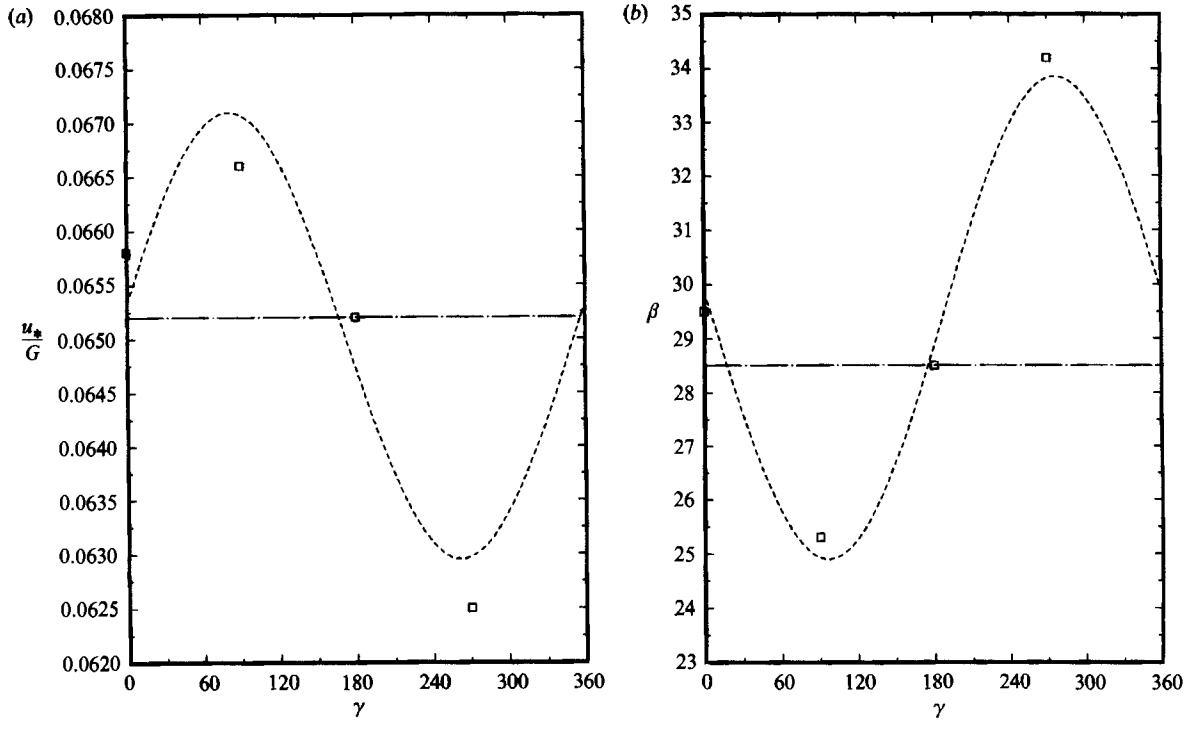

FIGURE 20. Variation with geostrophic wind orientation of (*a*) surface friction velocity and (*b*) surface shear angle at 45° latitude with $Re = 400$. –·– A90; ———, $c_1 + c_2 \cos\gamma + c_3 \sin\gamma$ interpolant, constants used are $(c_1, c_2, c_3) = (0.0650, 0.0003, 0.0020)$ for u_*/G and $(29.38, 0.50, -4.45)$ for β; symbols are results from cases A45E, A45W, A45N, and A45S.

longitudinal vortices. The DNS results thus corroborate Mason & Thomson's earlier LES results concerning this issue. Rolls were absent from the fields at all latitudes and wind directions. (Linear stability analysis hints that turbulent rolls might be more apt to appear in some of the simulations than in others. This is because, as pointed out by Leibovich & Lele, for certain orientations of Ω_H and G the horizontal rotation component can act to broaden the range of unstable wavenumbers, implying that no single wavelength has a distinct advantage during any mode selection process which might occur. A final coherent state is thus less likely. Other Ω_H–G configurations presumably act to narrow the wavenumber range, leading to the opposite effect.) The inflectional instability apparently does not lead to permanent longitudinal rolls. It may be important, however, in permitting transition to occur at lower Reynolds numbers than in the two-dimensional boundary layer. Buoyantly unstable conditions are probably required for large-scale PBL structures to arise and subsist. We plan to use a modification of the present code to stimulate the buoyantly unstable Ekman layer; such simulations will be reported later.†

For the neutral case, based on observations of the simulated fields (and especially the lack of longitudinal rolls) it appears that the turbulent Ekman layer has more in common with the turbulent two-dimensional boundary layer than with the quasi-laminar Ekman layer.

† *Note added in proof*: Recent computations have shown that the rolls do appear for a certain range of surface heating conditions (publication forthcoming).

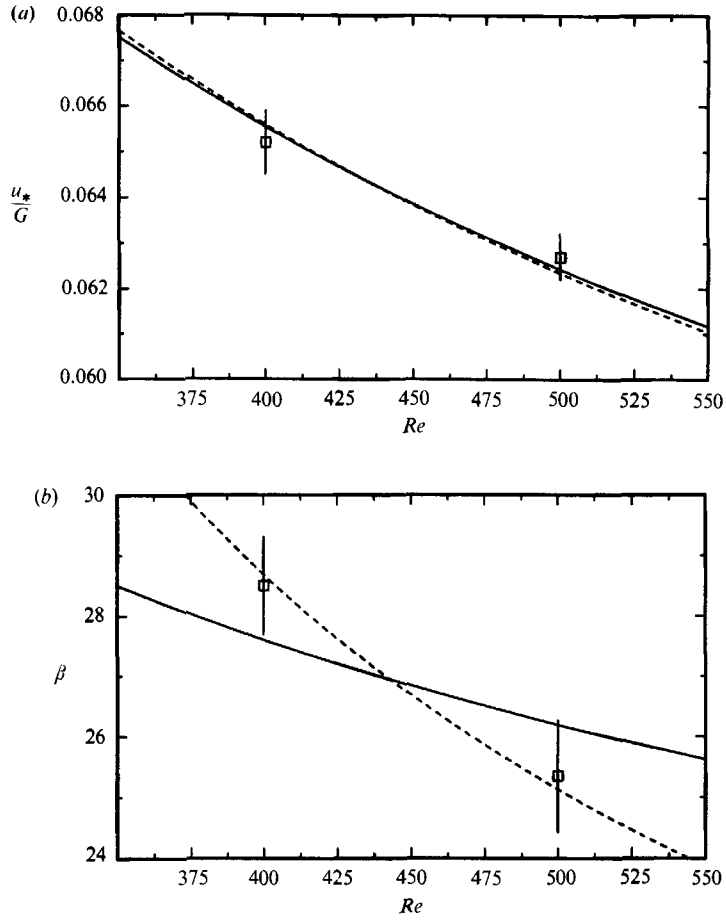

FIGURE 21. Comparison of basic similarity theory, higher-order correction and numerical results for (*a*) surface friction velocity and (*b*) surface shear angle (vertical scale expanded to facilitate comparison). ——, basic theory (Csanady 1967) with $A = 7.1, B = -0.7$, and $\kappa = 0.41$; – – –, higher-order theory (Spalart 1989) with $A = 5.2, B = 0.1, \kappa = 0.41$ and $C_5 = -52$; symbols are results from cases A90 and B90.

6.2. *Extrapolation to higher Re*

The $Re = 400$ and 500 90° latitude DNS data may be used in conjunction with asymptotic similarity theory to predict the variation with Reynolds number of u_* and β. The theory developed by Csanady (1967), and others, maintains that for smooth surfaces

$$\frac{G}{u_*}\cos\beta + \frac{2}{\kappa}\ln\frac{G}{u_*} = \frac{2}{\kappa}\ln Re - \frac{1}{\kappa}\ln 2 + B, \quad \sin\beta = \frac{A}{G/u_*}, \tag{5a,b}$$

where A and B are non-dimensional constants. When the DNS results are used to determine the similarity constants, we find that $A = 7.1$ and $B = -0.7$ provides the best overall fit of the variation of u_* and β from $Re = 400$ to 500. The accuracy of the fit is shown graphically by the solid curve in figure 21. The symbols are the DNS data points and the vertical lines through the symbols represent a measure of the uncertainty of the values, as discussed in §5. While the prediction for u_* is adequate,

that for β is not. Since the similarity constants have essentially no effect on the slope of the curves, other choices of A and B would lead to no improvement, so the theory represented by (5) evidently does not apply at these low Reynolds numbers.

In an attempt to expand the range of application to low Reynolds numbers, a higher-order theory has been developed by Spalart (1989). Originally derived for the boundary-layer flow with rotating freestream velocity, the theory uses arguments which are equally valid for the Ekman layer. The higher-order relationships are

$$\frac{G}{u_*}\cos\theta+\frac{2}{\kappa}\ln\frac{G}{u_*}=\frac{2}{\kappa}\ln Re-\frac{1}{\kappa}\ln 2+B, \tag{6a}$$

$$\sin\theta=\frac{A}{G/u_*}, \tag{6b}$$

where

$$\theta=\beta+\frac{2C_5}{Re^2}\left(\frac{G}{u_*}\right)^2. \tag{6c}$$

C_5 is a non-dimensional constant, analogous to κ (Spalart 1989). The only difference between (5) and (6) is the replacement in (6) of β with the modified angle θ, given by (6c). At high Reynolds numbers, θ approaches β, and the formulations become identical.

For the rotating freestream boundary-layer flow, Spalart (1989) found the higher-order prediction and surface-stress behaviour to match very well for Reynolds numbers $Re = U/(\frac{1}{2}\nu\hat{f})^{\frac{1}{2}}$ ranging from 500 to 767, where U is the magnitude, and $\hat{f}$ the rate of rotation, of the freestream velocity. In the present flow, over the smaller Re = 400 to 500 range, the agreement is also quite good, as shown by the dashed curve in figure 21. The constants used are $A = 5.2$ and $B = 0.1$, with C_5 taken to be -52. The exact value of C_5 is uncertain, but is thought to lie between -52 and -64 (Coles 1968; Spalart 1989). While Spalart found that $C_5 = -64$ gave the best results for the rotating freestream flow, we find that -52 produces the best fit. However, any value of C_5 between -52 and -64 used in the higher-order theory yields a much better prediction at these Reynolds numbers than does the unmodified theory (5).

The matching of the prediction and the data between the two DNS Reynolds numbers allows us to extrapolate the behaviour of u_* and β to arbitrary Reynolds numbers. Such an extrapolation is shown in figure 22. The error which would result from using the basic theory (solid curve) rather than the higher-order theory (dashed curve) is apparent, especially in the prediction for β. An indication of the range of Reynolds numbers over which the higher-order correction is significant is given by the difference between the dashed and dotted curves in figure 22. The dashed curve is the higher-order prediction and the dotted that of the basic theory using the higher-order constants ($A = 5.2, B = 0.1$).

Normally, a similarity theory valid for flow over rough surfaces is used in atmospheric applications in which a characteristic roughness height, z_0, appears, rather than the viscous length ν/u_*. The values of A and B obtained for use in (6) consequently might seem to have limited applicability. A connection can be made, however, between the rough and smooth surface constants. For a rough surface, the constants are (Csanady 1967)

$$B_{z_0}=G_x/u_*-\frac{1}{\kappa}\ln\frac{u_*}{fz_0}, \tag{7a}$$

$$A_{z_0}=G_y/u_*, \tag{7b}$$

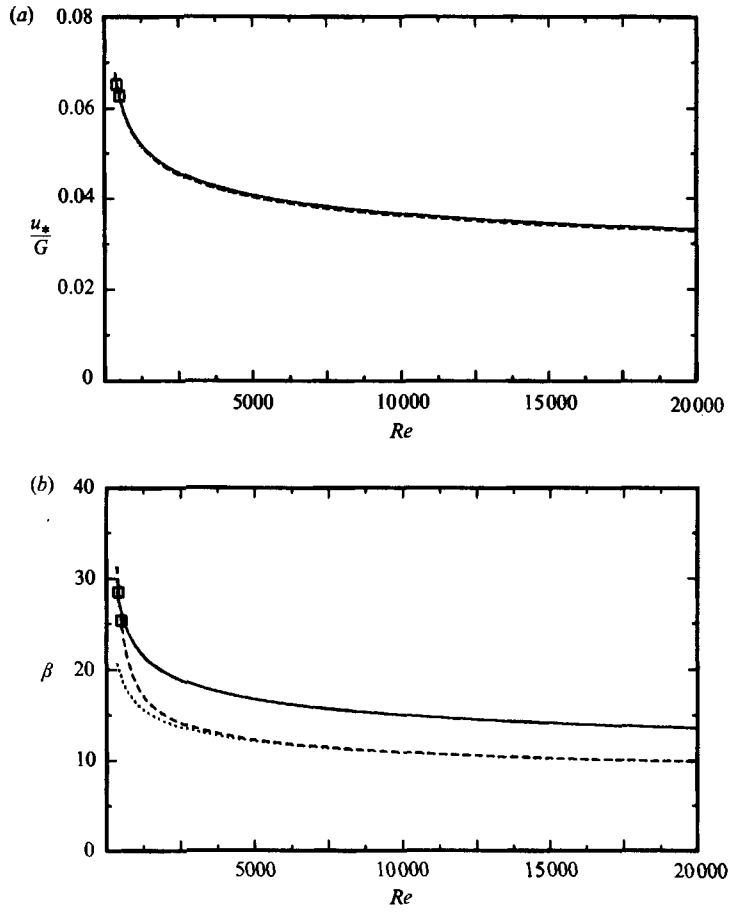

FIGURE 22. Extrapolation of (*a*) surface friction velocity and (*b*) surface shear angle with Reynolds number. ——, basic theory (Csanady 1967) with $A = 7.1$, $B = -0.7$, and $\kappa = 0.41$; – – –, higher-order theory (Spalart 1989) with $A = 5.2$; $B = 0.1$, $\kappa = 0.41$ and $C_5 = -52$; · · ·, basic theory (Csanady 1967) with $A = 5.2$, $B = 0.1$, and $\kappa = 0.41$ (dashed and dotted curves overlap in (*a*)); symbols are results from cases A90 and B90.

G_x and G_y being components of the geostrophic wind in a coordinate system at angle β (or θ for the higher-order theory) to the freestream velocity. By rearranging (6), we may write the smooth-surface constants in a similar form:

$$B = G_x/u_* - \frac{1}{\kappa}\ln\frac{u_*^2}{fv}, \tag{6a'}$$

and

$$A = G_y/u_*. \tag{6b'}$$

This implies that

$$A_{z_0} = A, \tag{8a}$$

and

$$B_{z_0} = B + \frac{1}{\kappa}\ln\epsilon, \tag{8b}$$

where

$$\epsilon = z_0/(\nu/u_*), \tag{8c}$$

the ratio of the routh- to smooth-surface lengthscales. We may therefore determine A_{z_0} directly from the smooth-surface DNS results and if we can specify ϵ such that

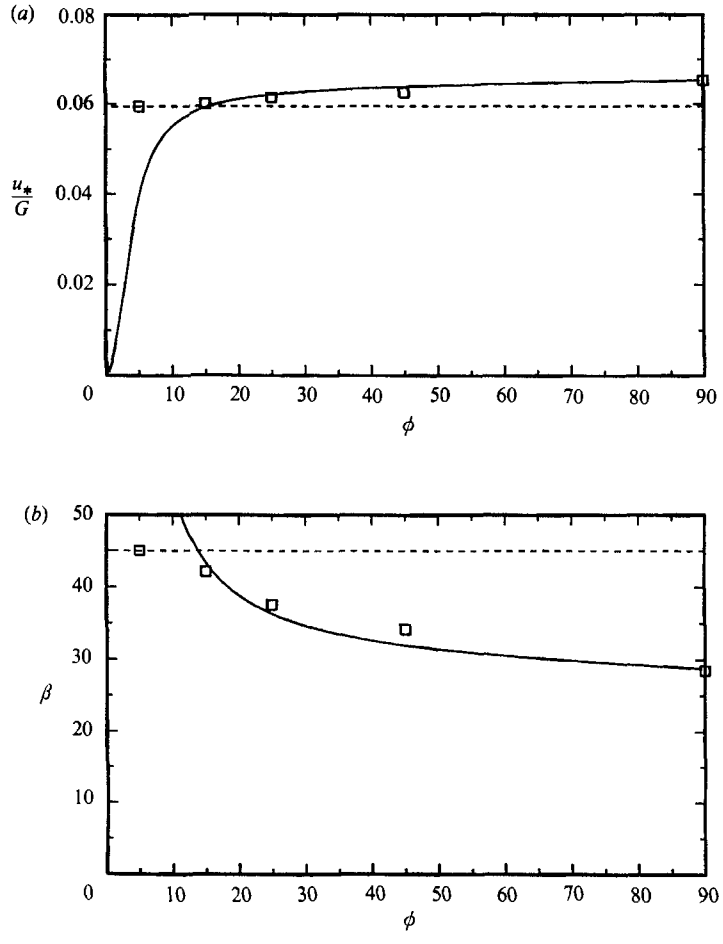

FIGURE 23 (*a*, *b*). For caption see facing page.

the outer regions of the flows over smooth and rough surfaces are identical, B_{z_0} as well. There is an extreme amount of scatter in the values cited in the literature, with $4 \leqslant A_{z_0} \leqslant 16$ and $-12 \leqslant B_{z_0} \leqslant 4$ (Caldwell *et al.* 1972; Wyngaard, Cote & Rao 1974; McBean 1979). The present DNS results imply $A_{z_0} = 5.2$ and, with ϵ taken to be 0.1, $B_{z_0} \approx -5.5$.

6.3. *Effect of latitude*

The greatest influence of the latitude–wind angle effect is noted when the wind is directed nearly due east or west. Differences as large as 20 and 70% in u_*/G and β, respectively, are found among the cases simulated. There is a 6 and 30% difference between these quantities at $\phi = 45°$ caused by changes of the wind direction alone (see figure 20). The magnitude of the effect is comparable to Mason & Thomson's observation of 4 and 21% differences in 45° and 90° latitude LES results. The degree to which system rotation can fundamentally modify a turbulent flow is also indicated by the observed variation with ϕ and γ of the structure parameter profiles (figure 16).

The explanation of why such an apparently small influence as the horizontal rotation has such a dramatic effect lies in the role of rotation in redistributing the energy among the individual components of the turbulent kinetic energy (Johnston,

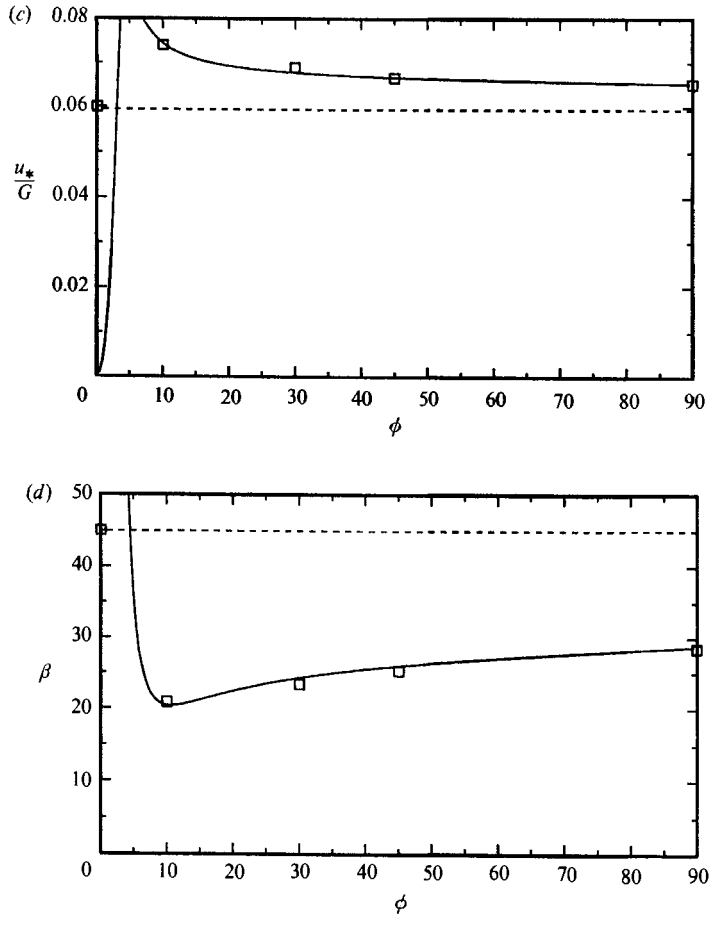

FIGURE 23. Surface shear variation with latitude at $Re = 400$ for (*a*), (*b*) west wind ($\gamma = 270$) and (*c*), (*d*) east wind ($\gamma = 90$) cases. ——, equation (10); – – –, laminar values; symbols are DNS results. In (*c*), the model predicts a maximum of 0.088 at $\phi = 4.5°$.

Halleen & Lezius 1972; Tritton 1978; Bardina, Ferziger & Reynolds 1983). The Coriolis force associated with Ω_H produces a source term

$$2\Omega_H(\langle w^2\rangle - \langle u^2\rangle) \tag{9}$$

in the dynamic equation for $\langle -uw\rangle$. Here the velocity components u and w are defined with respect to freestream axes and Ω_H is positive when it has the same sense as the rotation inherent in the shear. Throughout the Ekman layer the streamwise velocity fluctuations, $\langle u^2\rangle$, are significantly larger than the vertical, $\langle w^2\rangle$, (see figure 12*a*) so (9) implies that the tendency of positive Ω_H is to reduce, and a negative Ω_H to increase, $-\langle uw\rangle$. A change in $-\langle uw\rangle$ leads to a change in production of turbulence energy. Therefore, although the horizontal rotation has no direct effect on the magnitude of the total disturbance energy (no term containing Ω appears in the turbulence energy transport equation) it does change the disturbance energy level indirectly by modifying, through component redistribution, the Reynolds stress and hence the mean velocity profile and turbulence energy production. Specifically, positive Ω_H will reduce, and negative Ω_H will increase, the transfer of energy to the

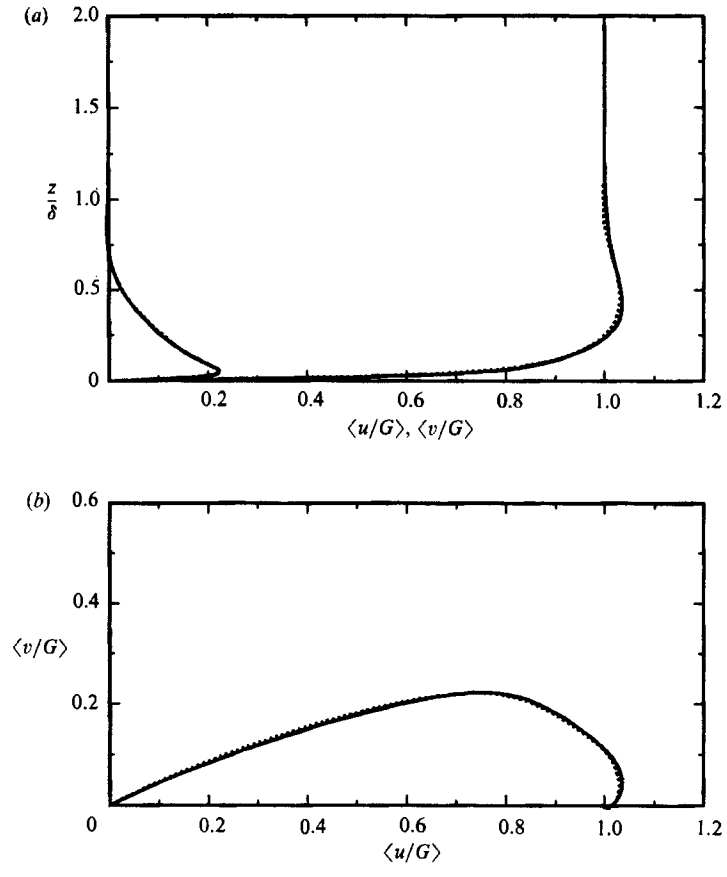

FIGURE 24. Comparison of case B90 with rotating freestream velocity boundary layer (Spalart 1989). Mean velocity (*a*) in axes aligned with freestream velocity, (*b*) hodograph; ——, B90; · · ·, Spalart.

turbulence so long as the streamwise velocity fluctuations are greater than the vertical. However, since rotation terms also appear in the $\langle u^2 \rangle$ and $\langle w^2 \rangle$ dynamic equations, this will not necessarily be true for Ω_H of any magnitude. Positive Ω_H reinforces, and negative Ω_H diminishes, the $\langle w^2 \rangle - \langle u^2 \rangle$ difference. This implies that positive rotation of any magnitude will reduce the turbulent energy level, but only a finite range of $\Omega_H < 0$ will lead to an increase. The upper bound on this range where negative Ω_H (locally) enhances the turbulence is the point at which the rotation rate is equal to half the spanwise vorticity (Tritton 1978).

The DNS results are consistent with these considerations. Positive Ω_H corresponds to wind from the west, so that the shear 'rolls with' Ω_H, and west wind cases are indeed found to become less energetic with decreasing ϕ (i.e. increasing Ω_H). East wind (negative Ω_H) simulations show the opposite effect, until very near $\phi = 0$, where Ω_H becomes so large as to switch from the production to suppression role, so that the turbulence collapses. It is observed that the maximum turbulent kinetic energy production rate (normalized by u_* and δ) for case A45E is 70% greater than that for A45W, while the rate for A10E is ten times that for A15W. A rule of thumb suggests that the effect on turbulence of some of the 'extra strains' such as rotation is an order of magnitude larger than the term representing the effect in the Reynolds-

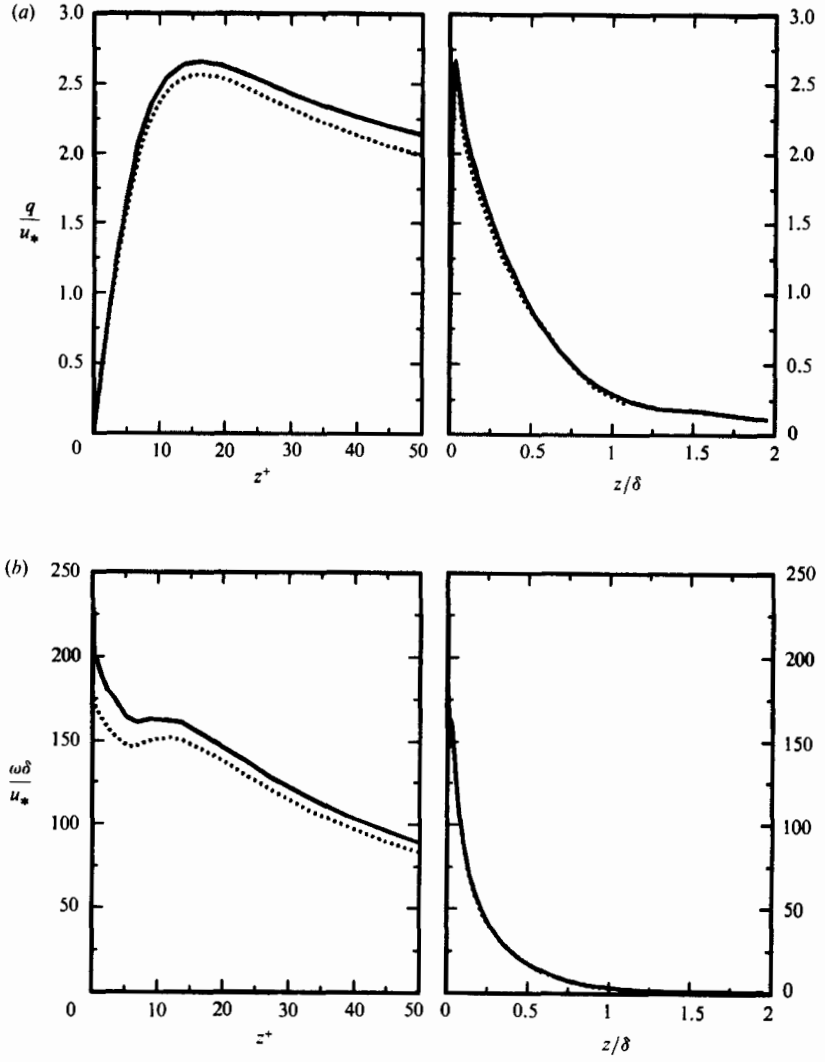

FIGURE 25. Comparison of case B90 with rotating freestream velocity boundary layer (Spalart 1989). Total r.m.s. fluctuations of (*a*) velocity (*b*) vorticity profiles; ——, B90; · · ·, Spalart.

averaged Navier–Stokes equations (Bradshaw 1973). The results presented here support this guideline.

Within the turbulent Ekman layer, the Rossby number $Ro = u_*/\delta f$ is the ratio of Coriolis to 'frictional' forces at the large scales. The definition of δ implies that $Ro \equiv 1$. This indicates that rotation significantly influences the large scales at any Reynolds number. We conclude that the 'f-plane' approximation, in which the horizontal rotation component is neglected, is not appropriate for the Ekman layer. Turbulence closures of the Reynolds-averaged momentum equations should include information about both the latitude and direction of the geostrophic wind.

6.4. *A general model*

A simple model giving u_*/G and β as functions of latitude, geostrophic wind orientation and Reynolds number may be derived by repeating the steps leading to

the asymptotic similarity theory for the case of arbitrary ϕ and γ. The resulting expressions are identical to (6) with A and B now depending on ϕ and γ. We assume that A and B can be fit by interpolants of the form $D_1(\phi)+D_2(\phi)\cos\gamma+D_3(\phi)\sin\gamma$ (cf. figure 20). For purposes of modelling we chose to represent $D_i(\phi)$ by simple functions of $\cot\phi$. This is based upon consideration of the flows with identical G, f and ν (and therefore Re) at various latitudes, and the fact that $2\Omega_H = f\cot\phi$. Physically, the influence of the rotation on the turbulence is assumed to be given solely by the components of Ω_H parallel and perpendicular to G. Near $\phi = 90°$ (where we must have smooth variations of $A(\phi,\gamma)$ and $B(\phi,\gamma)$) a Taylor series in the variables $\cot\phi\cos\gamma$ and $\cot\phi\sin\gamma$ is thus appropriate. This implies that near $\phi = 90°$, the interpolation coefficients must behave as follows: $D_1(\phi)-D_1(90) \propto \cot^2\phi$ and $D_{2,3} \propto \cot\phi$. We assume the simplest functions of $\cot\phi$ that have this form and fit the DNS results. A tentative model is therefore

$$g(\phi,\gamma) = E_1+E_2\cot^2\phi+(E_3\cos\gamma+E_4\sin\gamma)\cot\phi, \tag{10}$$

where g is A or B. The coefficients which best fit the data, determined by applying least-squares criterion to the (turbulent) A-series results, are $(E_1, E_2, E_3, E_4) = (5.24, 0.07, 0.12, -0.77)$ for A and $(0.18, -0.03, -0.14, -0.19)$ for B. Equation (10) may be used (away from the equator, $\phi = 0$) in conjunction with (6) to predict u_*/G and β as functions of Re, ϕ, and γ for the neutrally stratified turbulent Ekman layer over a smooth surface. Equation (8) may then be used to estimate the rough-surface constants.

The fit of the model to the $\gamma = 90$ and 270, $Re = 400$ DNS results is given by the solid curves in figure 23. Symbols represent simulation results, and dashed lines, laminar values. Note how the opposite effects by rotation of turbulence enhancement and suppression associated with the two wind directions is captured in the latitude variation, and that as ϕ approaches zero (so that B tends toward infinity) the drag coefficient given by the model for both $\gamma = 90$ and 270 approach zero (see equation (6)). The model is thus not valid near $\phi = 0$, or at any latitude for which the predicted u_*/G is less than the laminar value. While the vanishing drag coefficient is not qualitatively correct, it is at least consistent with the tendency toward laminarization expected as $|\Omega_H| \to \infty$. Ideally, one would derive an asymptotic theory for small latitudes. Unfortunately, it is not clear which flow should be specified at $\phi = 0$, where $f = 0$. Consequently, the singular behaviour as $\phi \to 0$ is not an argument against the model based on powers of $\cot\phi$.

An alternative model based on powers of $\cos\phi$, rather than $\cot\phi$, was also considered. Although exhibiting the expected variation near $\phi = 90$, where $\cos\phi \approx \cot\phi$, this model was unable to fit the data as well as the cotangent version, especially at low latitudes.

As discussed above, the ratio of the horizontal rotation to the vertical shear represents the relative importance of system rotation on the flow. Because the shear scales with $G/\delta = Gf/u_*$ (at least in the outer region, where the rotation is felt most strongly) and since $2\Omega_H = f\cot\phi$, the rotation/shear parameter is proportional to $(u_*/G)\cot\phi$. At fixed ϕ and γ, u_*/G (and thus the parameter) $\propto 1/\ln Re$ (see equation 6*a*)), which implies that the tendency toward laminarization with decreasing ϕ will slowly reduce with increasing Reynolds number. This is mirrored in the model by the fact that the latitude at which the laminar and predicted drag coefficients are equal slowly drops as Re grows (with $\gamma = 270$, this occurs at about $\phi = 15°$ for $Re = 400$, and at $\phi = 5°$ for $Re = 1500$). The range of validity is therefore expected to increase with increasing Reynolds number. The model should probably be used only for

latitudes about 5° greater than the laminar-prediction cross-over ϕ. For the case displayed in figure 23(*a*, *b*), the recommended range is thus $\phi \geqslant 20°$. In practice, the model is likely to be of little use at very low latitudes, since it is based upon the neutrally-stratified Ekman layer, which is never a valid approximation of the equatorial PBL.

6.5. *Comparison with a related flow*

It is interesting to compare some 90° latitude Ekman-layer results to those from another three-dimensional boundary layer. The turbulent flow in which the freestream velocity vector with magnitude U (not the entire system) rotates steadily at rate $\hat{f}$ has been simulated by Spalart (1989) at Reynolds numbers $Re = U/(\frac{1}{2}\nu\hat{f})^{\frac{1}{2}} =$ 500, 620 and 767. This flow and the present one have identical laminar solutions. Our $Re = 500$ results are compared in figures 24–25 with Spalart's corresponding $Re =$ 500 values (indicated by the dotted curves). The mean velocity profiles are shown in figure 24. The agreement is quite striking, especially for the hodograph in light of the differences between the $Re = 400$ and 500 cases, and the latitude effect, discussed above. Similar agreement exists in the (total) r.m.s. velocity and vorticity curves of figure 25. A major difference between the flows is that turbulence is not sustained in Spalart's flow at $Re = 400$. This may be due to the physical difference that, with the freestream velocity continually rotating, no fixed direction of momentum transfer exists. No analogue of the quasi-laminar Ekman-layer rolls is expected. The constants required in the higher-order asymptotic theory for the Spalart flow are $(A, B) = (5.3, 0.4)$ compared to the $\phi = 90°$ Ekman-layer values of (5.2, 0.1). While the difference in the values of B might seem large, recall that B appears in equation (6) along with terms containing $2/\kappa$ times a logarithm. Therefore it is better to compare, not B, but rather $\exp(\frac{1}{2}\kappa B)$; the ratio of the values of this quantity is $\exp(0.15\kappa) \approx$ 1.06.

The authors wish to thank Neil Sandham of Stanford University for reviewing the manuscript, Dr S. Lele of NASA Ames Research Center for providing a version of his Ekman layer linear stability code for our use and Professor R. L. Street for valuable advice. We also appreciate the useful comments offered by Professors D. K. Lilly, J. W. Deardorff, and C. W. Van Atta. We found the referee's suggestions to be quite helpful, and are grateful for their effort. This work has been sponsored by the Office of Naval Research under contract N00014-86-K-0157; computer resources have been supplied by NASA Ames Research Center.

REFERENCES

BARDINA, J., FERZIGER, J. H. & REYNOLDS, W. C. 1983 Improved turbulence models based on large eddy simulation of homogeneous, incompressible, turbulent flows. Ph.D. dissertation, Mech. Engng Dept, Stanford University. Thermosci. Div. Rep. TF-19.

BRADSHAW, P. 1973 Effects of streamline curvature on turbulent flow. *AGARD-AG*-169.

BRADSHAW, P. & PONTIKOS, N. S. 1985 Measurements in the turbulent boundary layer on an 'infinite' swept wing. *J. Fluid Mech.* **159**, 105–130.

BROWN, R. A. 1974 *Analytical Methods in Planetary Boundary-layer Modelling*. Wiley and Sons.

CALDWELL, D. R. & VAN ATTA, C. W. 1970 Characteristics of Ekman boundary layer instabilities. *J. Fluid Mech.* **44**, 79–95.

CALDWELL, D. R., VAN ATTA, C. W. & HELLAND, K. N. 1972 A laboratory study of the turbulent Ekman layer. *Geophys. Fluid Dyn.* **3**, 125–160.

COLES, D. E. 1968 The young person's guide to the data. *Proc. AFOSR-IFP-Stanford conf. on computation of turbulent boundary layers, Stanford, CA, 18–25 Aug. 1968.*

CSANADY, G. T. 1967 On the 'resistance law' of a turbulent Ekman layer. *J. Atmos. Sci.* **24**, 467–471.

DEARDORFF, J. W. 1970 A three-dimensional numerical investigation of the idealized planetary boundary layer. *Geophys. Fluid Dyn.* **1**, 377–410.

DEARDORFF, J. W. 1972 Numerical investigation of neutral and unstable planetary boundary layers. *J. Atmos. Sci.* **29**, 91–115.

ETLING, D. & WIPPERMANN, F. 1975 On the instability of a planetary boundary layer with Rossby number similarity. *Boundary-layer Met.* **9**, 341–360.

FALLER, A. J. 1963 An experimental study of the instability of the laminar Ekman boundary layer. *J. Fluid Mech.* **15**, 560–576.

FALLER, A. J. 1965 Large eddies in the atmospheric boundary layer and their possible role in the formation of cloud rows. *J. Atmos. Sci.* **22**, 176–184.

JOHNSTON, J. P., HALLEEN, R. M. & LEZIUS, D. K. 1972 Effects of spanwise rotation on the structure of two-dimensional fully developed turbulent channel flow. *J. Fluid Mech.* **56**, 533–557.

LEIBOVICH, S. & LELE, S. K. 1985 The influence of the horizontal component of Earth's angular velocity on the instability of the Ekman layer. *J. Fluid Mech.* **150**, 41–87.

LE MONE, M. A. 1973 The structure and dynamics of horizontal roll vortices in the planetary boundary layer. *J. Atmos. Sci.* **30**, 1077–1091.

MCBEAN, G. A. (ed.) 1979 The planetary boundary layer. *WMO no.* 530, *Tech. Note no.* 165.

MASON, P. J. & THOMSON, D. J. 1987 Large-eddy simulations of the neutral-static-stability planetary boundary layer. *Q. J. R. Met. Soc.* **113**, 413–443.

MELANDER, M. V. 1983 An algorithmic approach to the linear stability of the Ekman layer. *J. Fluid Mech.* **132**, 283–293.

SPALART, P. R. 1986*a* Numerical simulation of boundary layers. Part 1. Weak formulation and numerical method. *NASA TM* 88222.

SPALART, P. R. 1986*b* Numerical study of sink-flow boundary layers. *J. Fluid Mech.* **172**, 307–328.

SPALART, P. R. 1988 Direct simulation of a turbulent boundary layer up to $R_\theta = 1410$. *J. Fluid Mech.* **187**, 61–98.

SPALART, P. R. 1989 Theoretical and numerical study of a three-dimensional turbulent boundary layer. *J. Fluid Mech.* **205**, 319–340.

TATRO, P. R. & MOLLO-CHRISTENSEN, E. L. 1967 Experiments on Ekman layer instability. *J. Fluid Mech.* **28**, 531–543.

TENNEKES, H. 1982 Chapter 2 of *Atmospheric Turbulence and Air Pollution Modelling* (ed. F. T. M. Nieuwstadt & H. Van Dop). Reidel.

TRITTON, D. J. 1978 Turbulence in rotating fluids. In *Rotating Fluids in Geophysics* (ed. P. H. Roberts & A. M. Soward). Academic Press.

WIPPERMANN, F. K., ETLING, D. & KIRSTEIN, H. J. 1978 On the instability of a planetary boundary layer with Rossby number similarity. *Boundary-Layer Met.* **15**, 301–321.

WYNGAARD, J. C., COTE, O. R. & RAO, K. S. 1974 Modeling the atmospheric boundary layer. In *Turbulent Diffusion in Environmental Pollution*, vol. 18A (ed. F. N. Frenkiel & R. E. Munn). Academic Press.